Exploring energy distribution of photon upconversion and downconversion luminescence in lanthanide-doped nanoparticles

BY

QIANG WANG

A THESIS SUBMITTED TO MACQUARIE UNIVERSITY

FOR THE DEGREE OF

MASTER OF RESEARCH

DEPARTMENT OF PHYSICS AND ASTRONOMY

MAY 2018

MACQUARIE University
SYDNEY·AUSTRALIA

Statement of candidate

I certify that the work in this thesis has not been previously submitted for a degree nor has it been submitted as part of requirements for a degree to any other university or institution other than Macquarie University.

I also certify that the thesis is an original piece of research and it was authored by myself. Help and assistance that I have received in the course of my research work and in the preparation of the thesis itself has been acknowledged appropriately.

In addition, I certify that all information sources and literature used in the course of this research is also indicated where appropriate in this record of my thesis.

_____

QIANG WANG

Acknowledgements

First and foremost, I would like to express my deep sense of gratitude to my supervisor Dr. Yiqing Lu and research staff Dr. Xianlin Zheng, who supported me throughout this project. None of this project would have been possible if not for their efforts.

I am also thankful to the admirable staff in the department of physics and astronomy for their help and encouragement.

I wish to acknowledge Macquarie University for awarding me the international MRes scholarship to support my research study.

I would like to thank my parents, and my family as a whole, for their love and support throughout this project and my life.

Last but not least, thanks to my friends, Yan Wang and Yueying Cao, for making me feel special and being there when I needed them.

Contents

Abstract

Lanthanide-doped nanoparticles exhibiting short-wavelength infrared (SWIR) luminescence have emerged as promising luminescent probes for advanced in vivo imaging with enhanced tissue penetration, sensitivity and resolution. However, a key bottleneck remains in the limited luminescence efficiency, which fundamentally stems from the complicated energy levels and transition pathways possessed by lanthanide emitters.

This work aims to perform a spectroscopic study on several lanthanide-doped nanoparticles to illustrate their detailed photon transfer and energy distribution processes. A luminescence spectroscopy system is first set up, allowing characterisation of broad emission spectra spanning the ultraviolet to the SWIR region. Then, Er- and Tm-activated nanoparticles are examined, and the energy transition processes corresponding to individual characteristic emission peaks are interpreted based on their measured energy level diagrams alongside the excitation-emission relations. Finally, the influence of doping concentrations as well as additional co-dopants are investigated to explore potential approaches to regulating the energy distribution.

The results obtained here may be exploited to engineer lanthanide-doped nanoparticles with concentrated SWIR emission for efficient in vivo optical imaging in the future.

1 Introduction

1.1 The use of fluorescence in medical imaging

Medical imaging is broadly used to diagnose and monitor diseases, guide surgical interventions and evaluate treatment efficacy. Today, numbers of medical imaging techniques, such as computed tomography (CT), magnetic resonance imaging (MRI), positron emission tomography (PET), single-photon emission computed tomography (SPECT), and ultrasonography have been developed to probe both structural and functional information of the imaged subject. However, these techniques suffer from disadvantages of hazardous ionizing radiation (CT, PET, and SPECT), moderate sensitivity (MRI, ultrasonography), and reconstruction-dependent poor temporal resolution (PET, SPECT) to visualize molecular-level dynamics [1].

In contrast, fluorescence imaging does not have the same drawbacks and instead provides the capability of real-time wide field image acquisition with the diffraction-limited spatial resolution for long-term observation in living organisms [2]. The combination of far red and near-infrared (NIR) fluorescent dyes bound to polymer carriers, for example, can serve as a suitable platform for the simultaneous observation of the biodistribution and accumulation of the drugs and polymer carriers in solid tumours [3]. The fundamental advantages of using fluorescence imaging in biomedical research include its accessibility to 1) interactions between light and tissue, and 2) the corresponding photophysical and photochemical processes at the molecular level.

To perform fluorescence imaging in vivo, nontoxic fluorophores (i.e. fluorescent probes) are first injected into the patient's body, targeted to accumulate at the pathological tissue. Then, excitation light with a specific wavelength or wavelength range penetrates through tissue layers to reach fluorophores, pumping them onto the excited state. On their subsequent return to the ground state, the fluorophores emit photons at another specific wavelength different from that of the excitation light. In this way, existence and information of the pathological tissue can be extracted from the emission light characteristics.

Fluorescence imaging directly passing through the intact body part would be ideal. However, the commonly employed visible and UV light surfers from poor penetration to biological tissue. It is because the inhomogeneous components of the tissue, such as water, lipid membrane and subcellular organelles, cause serious photon scattering. Meanwhile, many endogenous biological molecules, such as haemoglobins, absorb light strongly and turn photons into heat dissipation [4, 5].

1.2 Biological transparent windows in NIR/SWIR region

To overcome this problem, much effort has been made to develop near-infrared (NIR) imaging agents in "biological transparency windows". However, the traditional NIR window (750-950 nm) is not optimal because background noise such as biological autofluorescence is still strong. As a result, tissue penetration depth is limited to 1 cm. Later in 2003, people found in the simulation that it would be possible to improve the signal-to-noise ratio by using fluorophores that emit light around 1320 nm instead of 850 nm [6]. Since then, a lot of interests have been focussing on developing new biocompatible fluorescent probes and applications with excitation/emission bands in the short-wavelength infrared (SWIR) window: 1000-1800 nm [7, 8]. Bashkatov et al. [5] proposed a formula to calculate the tissue penetration ability which is governed by tissue's absorption and scattering properties:

$$\delta = \left(3\mu_a\left(\mu_a + \mu_s\right)\right)^{-1/2} \tag{1.1}$$

Where μ_a is the absorption coefficient, μ_s is the scattering coefficient, and δ is the resulting penetration depth. They all vary with the optical wavelength.

It is found that wavelengths in SWIR window have much smaller scattering coefficient than wavelengths in NIR window (Figure 1.1.1 A). Except for the narrow absorption band of water centred at 1450 nm, the entire SWIR region has still low water absorption (Figure 1.1.1 C) and almost non-absorption of major light absorbers in biological tissue (Figure 1.1.1 B). Additionally, autofluorescence created by tissue reaction decreases exponentially as wavelength becomes larger, reaching undetectable levels past 1500 nm (Figure 1.1.1 D) [9]. Therefore, the benefits of much-reduced photon scattering, low photon absorption and diminished tissue autofluorescence show that SWIR window can increase tissue penetration dramatically.

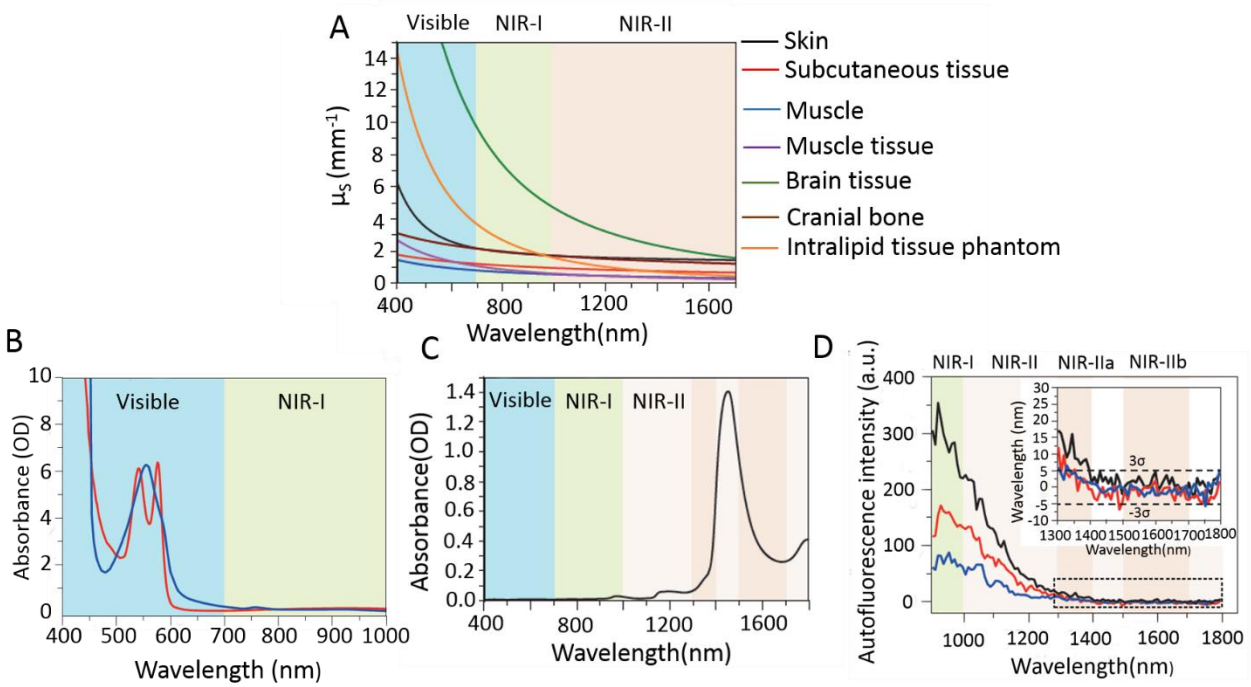

Figure 1.1.1. (A) Reduced scattering coefficients of different biological tissues as a function of wavelength which covers the visible, NIR (NIR-I) and SWIR (NIR-II) window. (B) Absorption spectra of oxyhaemoglobin (red) and deoxyhaemoglobin (blue) through a 1-mm long path in human blood. (C) Absorption spectra of water through a 1-mm-long path. (D) Autofluorescence spectra of ex vivo mouse liver (black), spleen (red) and heart tissue (blue) under 808 nm excitation light, reprinted with permission from [9], Copyright (2017) Springer Nature.

1.3 Probes and applications for NIR/SWIR imaging.

Expanding development of NIR fluorescence imaging techniques in preclinical and clinical trials is largely ascribed to the increasing number of choices of NIR fluorescent probes that can label various cells and organs. The recent progress in the fabrication of nanomaterials with excitation and emission in the NIR (750-950 nm) and SWIR (1000-1800 nm) windows fall in four main categories: organic small molecules, single-walled carbon nanotubes (SWCNTs), quantum dots, and lanthanide-doped nanoparticles.

1.3.1 Organic small molecules and its application of fluorescence imaging surgical system (FIGS)

Organic small molecules have advantages of fast excretion rate and are less retained in the organs, such as liver and spleen. Therefore, they are excellent for clinical translation. Indocyanine green (665

nm/692 nm) [10] and methylene blue (788 nm/813 nm) [11] are the first NIR fluorophores approved by US Food and Drug Administration (FDA) for biomedical applications in humans. The two fluorophores are widely used in the intraoperative visualization of anatomical features, including blood and lymphatic vessels. It is known some organic fluorophores also work in the SWIR window. In 2013, Tao et al. fabricated a SWIR contrast agent IR-PEG, by encapsulating an organic dye IR-1061 into polymer poly (acrylic acid) (PAA) matrix whose surface was subsequently PEGylated. The IR-PEG displayed strong fluorescence emission in the wavelength range from 900-1100 nm (Figure 1.2.1 A) [12]. In 2016, a small-molecule SWIR organic fluorophore (CH1055, 970 Da) was produced with the property of both superior biocompatibility and unprecedented body clearance. After conjugating to short PEG chains, CH1055–PEG displayed virtually no accumulation in the liver, with corresponding high level of renal clearance evidenced by >90% excretion through kidneys within 24 h (Figure 1.2.1 B) [13].

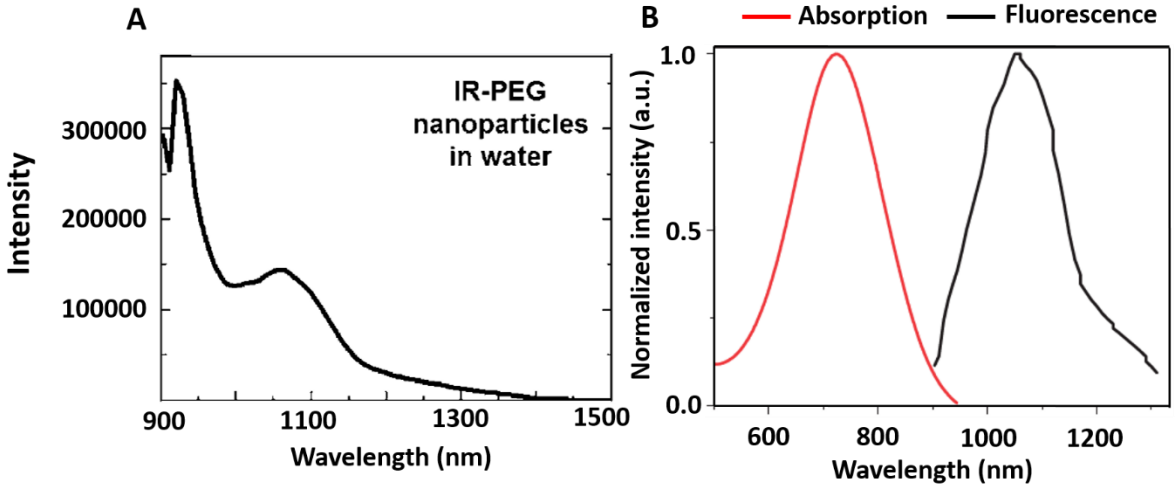

Figure 1.2.1. (A) SWIR fluorescence spectrum (excited by an 808 nm laser) of IR-PEG nanoparticles in water, reprinted with permission from [12], Copyright (2013) John Wiley and Sons. (B) Absorption and fluorescence spectrum of CH1055-PEG (excited by 808 nm laser), demonstrating an absorption peak at 750 nm and an emission peak at 1055 nm, reprinted with permission from [13], Copyright (2015) Springer Nature.

Clinical studies using the FDA-approved fluorophores Indocyanine green (ICG) and methylene blue (MB) as well as the IRDye800CW (excitation/emission 774/789 nm) [14, 15] have applied NIR fluorescence imaging in human patients for intraoperative localization of primary tumours during the actual surgery. The so-called fluorescence-assisted imaging surgical system (FIGS) can provide broadband visible-to-NIR illumination and multichannel image acquisitions in the NIR window. The diseased blood vessels and lymph nodes that are invisible to the naked eye or to traditional cameras

in the visible window can be distinguished clearly from benign tissues by the overlap of the visible image and NIR fluorescence image (Figure 1.2.2).

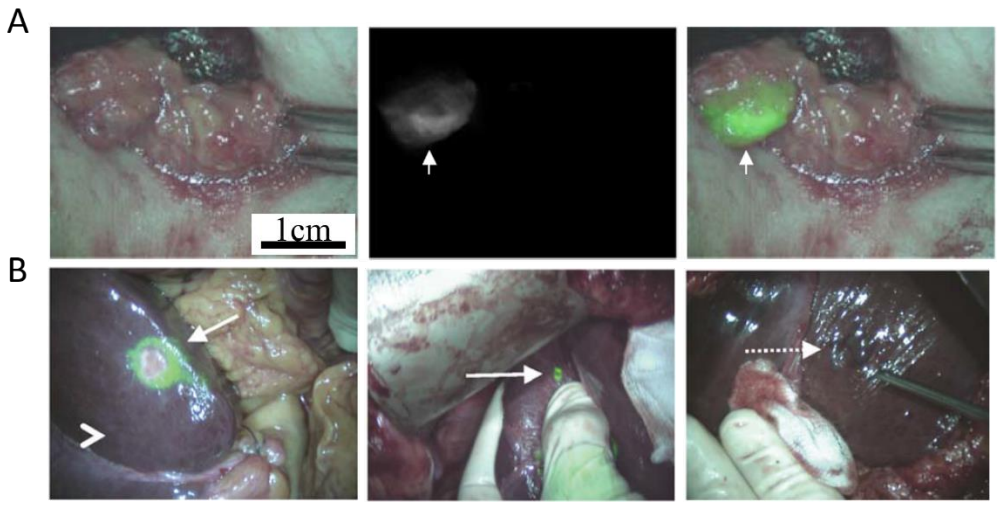

Figure 1.2.2. (A) Colour/NIR overlaid image showing a sentinel lymph node (white arrow) in a breast cancer patient injected with the ICG/HSA complex, reprinted with permission from [16], Copyright (2009) Springer Nature. (B) Colour/NIR overlaid images of a colorectal liver metastasis (left, indicated by the arrowhead), an occult metastasis (middle, indicated by the arrow) and a benign cyst (right, indicated by dashed arrow) in human patients injected with ICG, reprinted with permission from [17], Copyright (2013) John Wiley and Sons.

Although organic small molecular dye has good characteristics such as rapid excretion, good biocompatibility and cell targeting ability (through conjugation with specific targeting ligands), it still suffers from several disadvantages. First, it is difficult to control the excitation and emission wavelengths and tune them to precious values [18]. Second, the emission quantum-yield is usually less than 15% in the aqueous environment [18, 19]. Third, most conventional organic fluorophores are susceptible to photobleaching, which limits the application of long-term tracing [18, 19].

1.3.2 Single-walled carbon nanotubes and its application for in vivo vascular imaging

Single-walled carbon nanotubes (SWCNTs) have intrinsic fluorescence emission in SWIR window (1000-1800 nm). According to different synthetic routes, the SWCNTs show the different ranges of photoluminescence wavelengths [20-26], e.g. high-pressure CO (HiPco) decomposed SWCNTs (Figure 1.2.3).

To make SWCNTs suitable for fluorescence imaging with sufficient SWIR photoluminescence intensity, a considerable amount of effort has been paid to enhance the intrinsic fluorescence emission by applying surfactant exchange [27, 28], reducing the degree of bundling [29], and removing the

possible quencher from the surface of nanotubes [30]. With much-improved quantum yields of photoluminescence, the SWCNTs have shown great potential as contrast agents in a wide variety of in vivo biological applications because of its large Stokes shift of hundreds of nanometres and the much longer emission spectra than traditional fluorophores.

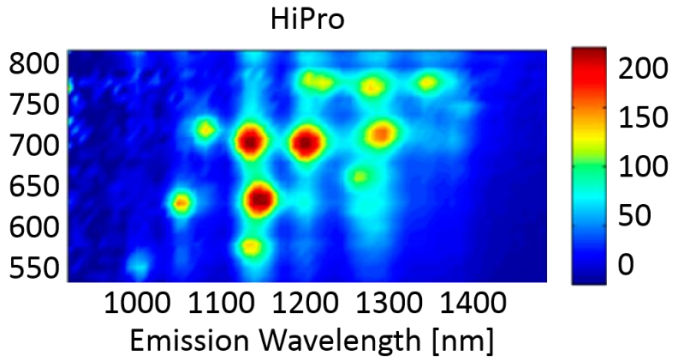

Figure 1.2.3. The plot of photoluminescence and excitation of SWCNTs, reprinted with permission from [26], Copyright (2015) American Chemical Society.

In 2012, Hong et al. performed SWIR fluorescence imaging for in vivo angiography by intravenously injecting a fluorophore comprised of SWCNT to the mouse hind limb vasculatures. The resolution of the SWIR fluorescence image is compared with the image of micro-CT, which is commonly used for 3D reconstruction of anatomical features based on the deeply penetrating X-ray. It has been found that the SWIR fluorescence imaging using SWCNT as contrast agent is able to resolve small hind limb vessels with widths down to 35 μm, which is approximately 3 times smaller than the resolution limit of micro-CT (Figure 1.2.4) [31].

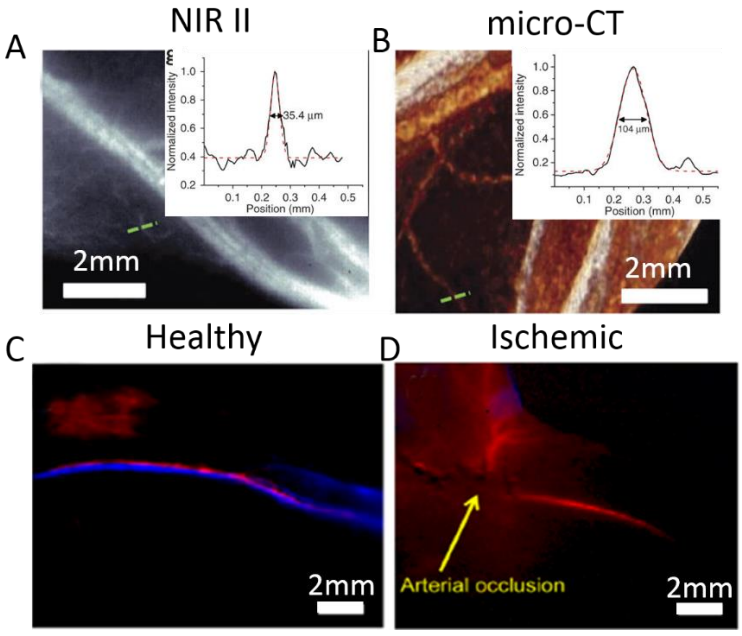

Figure 1.2.4. (A, B) Side-by-side comparison of mouse hind limb angiography obtained by SWIR (NIR-II) fluorescence imaging (A) and micro-CT imaging (B) of the same mouse. The inset shows the line intensity profile along the green dashed bar in each image. (C, D) The Colour/ SWIR overlaid images showing the arteries (red) and veins (blue) of a healthy mouse hind limb (C) and an ischemic mouse hind limb (D), reprinted with permission from [31], Copyright (2012) Springer Nature.

The major challenge for SWCNTs in clinical imaging and drug delivery applications is the potential long-term toxicity because SWCNTs without proper functionalization may aggregate and interact with cells inducing certain cell responses such as cell toxicity [32]. Although PEGylated SWCNTs exhibit excellent biocompatibility, their quantum-yield (QY) reduced significantly compared with that of surfactant-suspended SWCNTs, which become another major limitation for SWCNT-based fluorescence imaging [33]. Therefore, the surface coating and size of SWCNTs required to be optimized to maintain both biocompatibility and high QY.

1.3.3 Quantum dots and its application for Tumour-targeted imaging system

Quantum-confined nanoparticles or quantum dots (QDs) includes typical categories of II-VI (CdTe, HgTe), I-VI (Ag_2S, Ag_2Se), and III-V (InP, InAs, CuInSe, $AgInS_2$). Each category has shown its opportunity to create NIR or SWIR fluorescence probes.

For category II-VI, CdTe, HgTe are the most widely studied II-VI QDs in the NIR region. Alloying these materials within nanocrystal results in mixed $Cd_xHg_{1-x}Te$ particles. The control of the CdTe and HgTe QD sizes and the composition of alloyed $Cd_xHg_{1-x}Te$ QDs allowed us to tune the photoluminescence band in the wide spectral region from green to NIR [34-36]. For category I-VI, Ag_2S is reported to emit NIR light easily and has low toxicity to organisms. A lot of synthesis methods have been reported to render Ag_2S QDs become aqueous NIR QDs [37-39]. One of the examples is 6PEG-Ag_2S QD, synthesized by reacting Ag_2S-DHLA (dihydrolipoic acid) with amine-functionalized six-armed PEG. The spectrum of 6PEG-Ag_2S QD solution revealed that the emission was centred at 1200 nm, and the nanoparticle was stabilized in phosphate buffered saline (PBS) for over 0.5 h and remained over 50% of its initial photoluminescence intensity [38]. Category III-V includes InP, InAs and $InAs_xP_{1-x}$, which benefit from their narrow bandgap, but suffer from low quantum yields. To overcome this problem, plenty of efforts have been made in designing core-shell structures to enhance the QY [40, 41], such as the core-shell1-shell2 structures (InAs/CdSe/ZnSe) where the intermediate CdSe buffer layer decreases the strain between the InAs core and the ZnSe outer shell, which help improve the photoluminescence intensity. The final emission wavelengths can

be tuned from 885 to 1425 nm by tuning the core size and shell thickness [41]. By careful design of the core-shell structure and surface modification, the QDs demonstrate the good properties of tuneable emission wavelengths, photostability, high emission efficiency, with a handful choice of composition for in vivo biological imaging.

In 2016, Liu et al. developed their versatile bio-imaging probes (a core/shell structure of quantum dots ($CuInSe_2$/ZnS) conjugated with a tumour-specific homing peptide CGKRK, called QD-PEG-P) with good properties of long circulation time, photostability and low toxicity. According to their report, the probes exhibit strong tumour-specific homing property, the targeted probe clearly denotes tumour boundaries and positively labels a population of diffusely infiltrating tumour cells, suggesting its utility in precise tumour detection during surgery (Figure 1.2.5) [42].

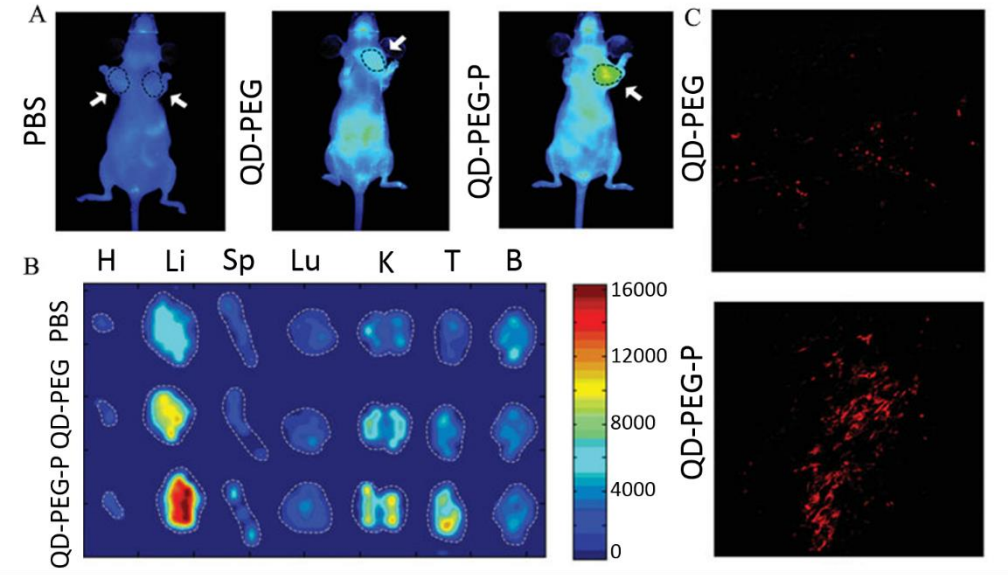

Figure 1.2.5. (A) Intravital whole-body fluorescent imaging of breast-tumour-bearing nude mice (700 nm excitation) at 28 h after intravenous injection of PBS, QD-PEG, or QD-PEG-P. White arrows show the position of tumours (B) Ex vivo imaging of the tissues harvested from the mice in (A) after the in vivo imaging. H, heart; Li, liver; Sp, spleen; Lu, lung; K, kidney; T, tumour; B, brain. (C) Representative confocal microscopy images of QD distribution in sections from the tumours in panel (B), reprinted with permission from [42], Copyright (2015) John Wiley and Sons.

Despite the superior optical properties, the toxic effects of QDs depend on many parameters including their composition, concentration, surface coating, size and synergistic effects [43]. Therefore, it is difficult to make QDs approved for different biological applications in the human body.

1.4 Lanthanide-doped nanoparticles as SWIR probes

1.4.1 Fundamental knowledge of lanthanide-doped nanoparticles

Lanthanide elements are spectroscopically rich species, including 15 chemical with atomic number from 57 to 71 elements (Er^{3+}, Tm^{3+} , Ho^{3+} , Pr^{3+} , Ce^{3+} , Nd^{3+} , Tb^{3+} , Dy^{3+} , Sm^{3+} and Eu^{3+}, etc.). The 4f orbitals of lanthanide ions are buried beneath the 6s, 5p, and 5d orbitals; hence, the spectra arising from f–f transitions are insensitive to the environment.

The typical lanthanide-doped nanoparticles are composed of three components: a host matrix, a sensitizer and an activator. The host matrix requires to be optically transparent and has low lattice phonon energy, which is the guarantee to minimize non-radiative losses and maximize radiative emission. Among various host materials, $NaYF_4$ has been widely recognized as one of the most efficient host lattices. The compound of $NaYF_4$ exhibits two types of crystallization phases: the α-type and β-type. The emission intensity of β-type material is higher than that of α -type material due to the enhanced electronic coupling caused by asymmetric structure (Figure 1.2.6) [44].

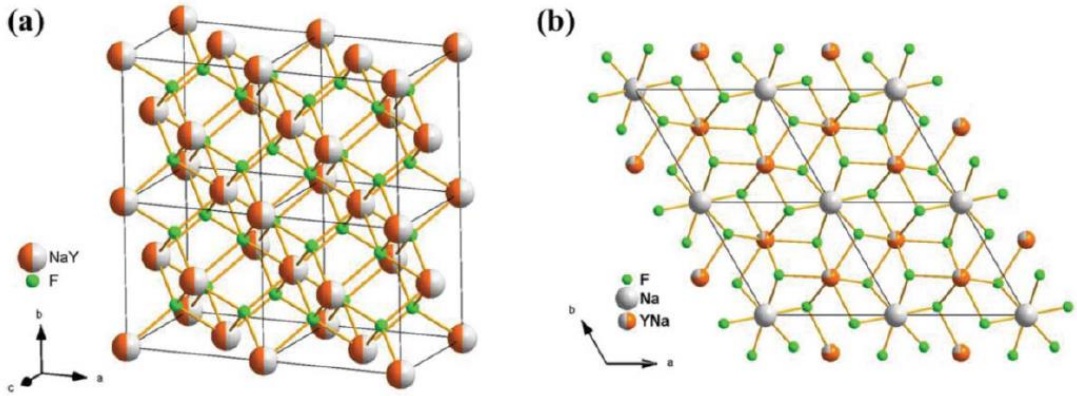

Figure 1.2.6. Crystal's structure of $NaYF_4$ phosphor: (a) α-type, cubic structure (b) β-type, hexagonal structure, reprinted with permission from [44], Copyright (2016) Taylor & Francis.

The sensitizer in the lanthanide-doped nanoparticle is responsible for transferring photon energy to the activator, therefore it should be able to absorb large photon energy and the energy levels should match those of activators. Among all the lanthanide ions, the Yb^{3+} ion is considered as the best sensitizer ion because the energy level of Yb^{3+} ion is quite simple, with only one excited state, $^2F_{5/2}$. The $Er^{3+,}$ Tm^{3+} and Ho^{3+} ions feature ladder-like energy levels to perform multiple-photon absorption process, therefore are thought as the best choice for activators [45]. When exciting lanthanide-doped nanoparticles by the light source, the sensitizer Yb^{3+} absorbs photons and transfers the energy to its neighbouring activators. The activators receive the energy and jump from ground state to the

metastable state. The activators continue to receive photon energy and jump from lower metastable state to higher metastable state as long as the gap energy between two metastable levels matches the photon energy transferred from Yb^{3+}, or relax back to the lower metastable levels or ground state to emit different wavelengths of fluorescence, the process of which is shown in Figure 1.2.7 [46-50].

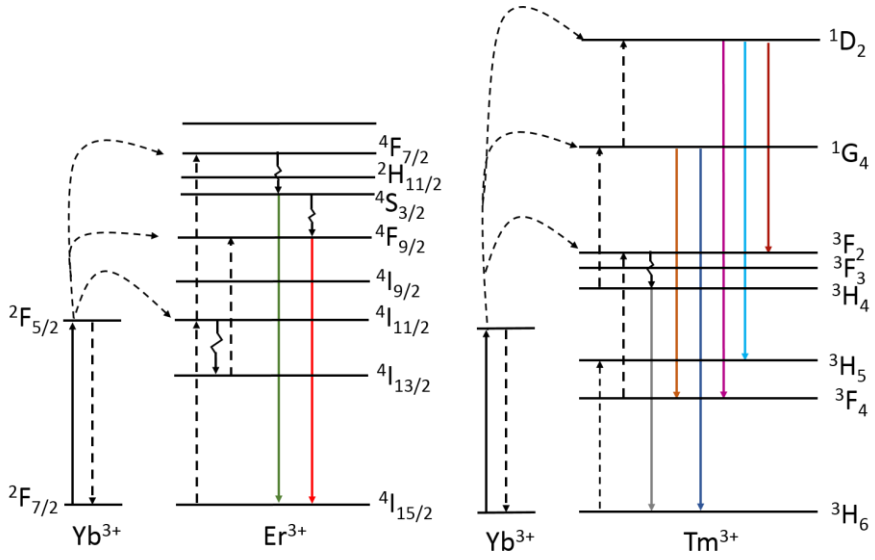

Figure 1.2.7. The simplified energy-level scheme of (Left) $NaYF_4$:Yb:Er nanocrystals and (Right) $NaYF_4$:Yb:Tm nanocrystals, indicating major energy levels, reprinted with permission from [48], Copyright (2014) American Chemical Society.

Due to the energy transition between two closed independent energy states, the lanthanide ions typically have emission line widths of 10 to 20 nm (FWHM, full width at half maximum), which is about half that observed for quantum dots (~25 to 40 nm) and much narrower than that observed for organic dyes (~30 to 50 nm) or transition metal ions (~100 nm), allowing more resolvable emission bands to be packed into the same spectral bandwidth [51]. Besides, the rich number of energy levels create a variety of emission wavelengths as well as large band shifting between excitation and emission [52]. Moreover, the morphology of core/shell structure can be well-developed to a uniform and monodispersed shape with size down to 10 nm [53]. The properties of spectra insensitive to the environment, exceptional photostability, controllable small size, large Stokes shift, and more resolvable emission bands have made lanthanide ions ideal as biomedical imaging agents for in vivo biological imaging [53-59].

1.4.2 Opportunities for Lanthanide-doped nanoparticles

In 2013, D.J. Naczynski et.al first demonstrated real-time multifunctional imaging system by using lanthanide-doped nanoparticles. In comparison to QDs and SWCNTs (detectable at 5 nM (nmol/L)

and 6 nM at excitation power of 0.14 W/cm^2), the lanthanide-doped nanoparticles show a higher detection sensitivity (detectable at 3 nM excitation power of 0.14 W/cm^2). The rapid circulation capability is confirmed by tracing lanthanide nanoparticles in mice body. The SWIR fluorescence intensity is identified in the tail vein (5s) before clearing the vasculature to enter the heart and lungs (10s) and become progressively intense in the liver and spleen (30s) (Figure 1.2.9 b). Except for vascular imaging ability, the lanthanide nanoparticles encapsulated by albumin ((RE)ANCs) also exhibit strong accumulation at tumour site due to both albumin-mediated active transport and enhanced permeation and retention effect (Figure 1.2.9 c).

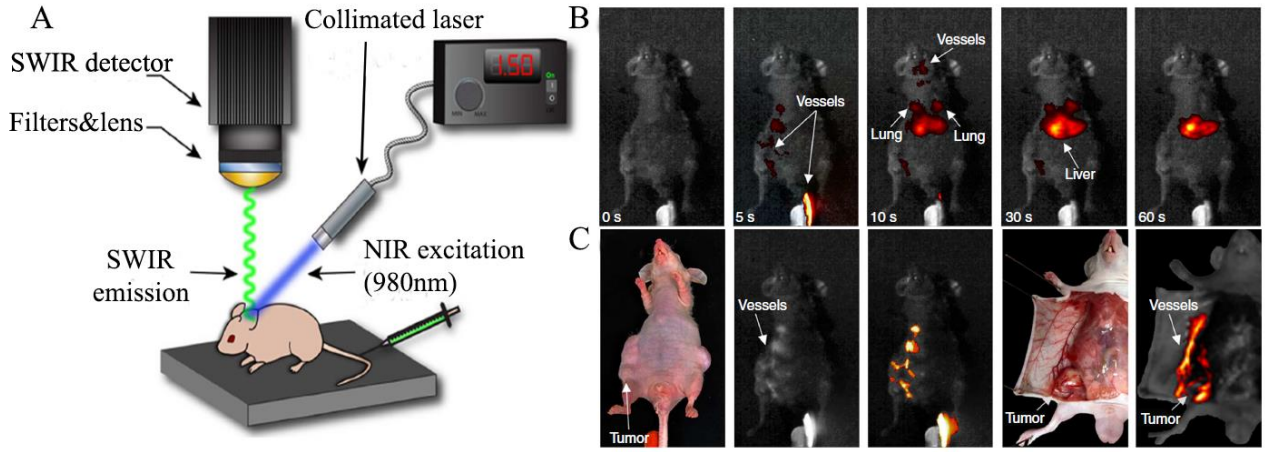

Figure 1.2.8. (A) Schematic of the portable SWIR imaging prototype. (B) Real-time, video-rate biodistribution of intravenously injected lanthanide nanoparticles captured in hairless mice using the imaging system prototype. (C) Nude mice bearing melanoma xenografts were intravenously injected with lanthanide nanoparticles and imaged near surrounding tumour regions, reprinted with permission from [58], Copyright (2013) Springer Nature.

The above experiment demonstrates the multifunctional imaging ability of lanthanide-doped nanoparticles. Since the lanthanide-doped nanoparticles are extremely resistant to photobleaching, the long-term in vivo detection can be easily realized. Furthermore, the lifetime of luminescence (hundred microseconds) is much longer than the lifetime of autofluorescence (tens of nanoseconds). By combining the time-gating signal acquisition method with lanthanide-doped nanoparticles, the emissions can be successfully separated from short-lived autofluorescence and scattering light. Without the interference of strong autofluorescence and scattering light, the imaging contrast will be enhanced dramatically [59].

Finally, the advantages and disadvantages of NIR/SWIR probes are summarized in Table 1.1

Table 1.1 The advantages and disadvantages of typical NIR/SWIR probes for biomedical imaging

Class	Probe name	Excitation/Emission	Advantages		Disadvantages	Reference
Organic small molecular	Indocyanine green(ICG)	807 nm peak/ 822 nm peak	Biocompatible, low toxicity, fast clearance rate	fluorescence-based intraoperative imaging	Adverse reaction at high dose, not optimal contrast agents	[10, [18]
	Methylene Blue(MB)	667 nm peak/ 686 nm peak				[11], [18]
	IRDye800CW	774 nm /789 nm		Conjugatable with targeting ligands	Persistently accumulate in the skin	[14], [15]
	IR-PEG	600-1500 nm /900-1400 nm		Photostability, small size	Low QYs (1.8% for IR-PEG in water, 0.3% for CH1055-PEG in water, PBS, serum)	[12]
	CH1055-PEG	750 nm peak/ 1055 nm peak		Strong tumor accumulation through nonspecific uptake		[13]
Carbon material	SWCNTs	550-1050 nm/ 1000-1800 nm	Large Stoke shift, electrical property, biocompatible and stable in blood after surface modification		Low QYs caused by surface modification	[25],]27]
QDs	6PEG-Ag2S	550-820 nm/ 1100-1700 nm	Photostability	Strong tumour accumulation through nonspecific uptake, biocompatible, soluble in blood	Retention in liver and spleen	[36]
	InAs/CdSe/ZnSe	UV-1300 nm /6001700 nm		High QYs(~50%), stable in water	Release of cadmium cause negative effects on cell viability	[40], [42]
	CuInSe2/ZnS-PEG-CGKRK	UV-550 nm/ 550-850 nm		strong tumor-specific targeting, long circulation half-life, low toxicity	Insignificant cell toxicity and retention in liver and spleen	[41]
Lanthanide-doped nanoparticles	NaYF4:Yb:Er3+, Ho3+,Tm3+ , Pr3+	808 or 980 nm/ 1000-1600 nm		High detection sensitivity, multi-spectra, long luminescence lifetime, biocompatible after encapsulated in HAS	Aggregation in aqueous solution without encapsulation	[58]

1.4.3 Research objectives

Despite the unique opportunities of lanthanide-doped nanoparticles, the intensity of their NIR/SWIR emission is still low. It is because the energy transition processes in lanthanide-doped nanoparticles which produce upconversion and downconversion luminescence could be changed under different excitation intensities. The complex multi-photon absorbing process and co-relaxation process also make it difficult to improve the quantity yields of specific-wavelength emission directly.

To improve the luminescence intensity in the NIR and SWIR region, the first objective of this project is to figure out the energy transition processes included in the lanthanide-doped nanoparticle. Second, the dominant energy transfer pathways (or co-relaxation pathways) will be investigated for each observed emission peak. Third, to realize the intensity enhancement, the modification of nanoparticles such as changing doping concentration, adding additional dopant will be trialled and the result will be compared with that of the original one to inspect the change of energy transfer pathways (or co-relaxation pathways) and effect on the energy distribution of emission wavelengths.

1.5 Thesis overview

My thesis consists of five chapter. This first chapter introduces the popular NIR/SWIR fluorescence probes and their applications for in vivo biological imaging, including the benefits of lanthanide nanoparticles for long-lifetime luminescence imaging.

In chapter 2, the design procedure of an optical system used to capture the entire spectra of lanthanide nanoparticles is introduced firstly. The spectrometer calibration and experiment methods are explained in the second and third part.

In chapter 3, two typical lanthanide nanoparticles Er- and Tm- doped $NaYF_4$:Yb are selected to measure their emission spectra using our designed system in the first step. Then, the corresponding energy transitions are calculated by searching two energy states which have the same energy value with luminescence peaks. Third, the possible energy transfer processes that populate the energy transitions are interpreted through the analysis of power-dependent luminescence intensity. Finally, the relative intensities of luminescence peaks are calculated and the possible factors that affect the energy distribution are explored based on the measured data.

In chapter 4, the high Tm concentration nanoparticle $NaYF_4$:20%Yb:4%Tm and new dopant nanoparticle $NaYF_4$:20%Yb:0.5%Tm, 2%Gd are compared with the original nanoparticle NaYF4:20%Yb:0.5%Tm to differentiate the influence on energy distribution of luminescence and to assess the weight of energy transfer pathways on supporting luminescence.

Finally, chapter 5 concludes the result of my work and give the description of my planned future work.

2

Instrumentation, experimental methods

This chapter reports the design and evaluation of a low-cost and ultra-broadband spectrum measurement system. In order to explore the relationship between emission wavelength and energy level of lanthanide-doped nanocrystals, a prototype system comprising cuvette holder, two different spectrum meters and excitation module employing 980 nm diode lasers is designed and constructed. Simultaneously this system is calibrated by using a specific wavelength in the overlapping spectrum range of two spectrum meters. After this, an effective experiment proposal including sample preparation and data acquisition is proposed.

2.1 System overview

The lanthanide doped nanocrystals can produce upconversion and downconversion luminescence from short wavelength infrared (SWIR) light to visible or ultraviolet (UV) light, because of the complex energy level structure [60]. In order to understand their photoluminescence mechanism for controlling their emission wavelengths or energy distribution efficiency, it is prerequisite that collecting the entire spectrum by an accurate spectrum measurement system. However, the current commercial spectrometer cannot measure the spectrum from UV to SWIR without changing any setup. My work in this chapter is to build a spectrum measurement system consisting of 980 nm excitation module, cuvette holder with four light ports, VIS spectrometer and NIR spectrometer, to capture the whole emission spectrum with minimum influence from the environment, such as ambient light.

2.1.1 System design

The lanthanide doped nanocrystals have very wide luminescence spectra, e.g. the emission wavelengths of NaYF4:Yb:Er range from 308 nm to 1800 nm, as shown in Figure 2.1.1 [61]. A single commercial spectrometer cannot cover the entire emission spectrum, which is caused by two major limitations: 1) The spectral response range of sensor is different, such as silicon CCD array and

InGaAs array (Figure 2.1.2); 2) the reflectivity or transmittance for different wavelengths depends on optical components' materials. To overcome this issue, I designed the spectrum collection module using two different spectrometers. One spectrometer #USB2000+ is used to cover the emission spectrum from 300 nm to 1100 nm. The other one #NIRQuest512 is used to cover the emission spectrum from 900 nm to 2200 nm. In addition, to excite the Yb:Tm or Yb:Er doped nanocrystals, an excitation module is designed by using 980 nm fibre-coupled laser diode, because of the high absorption efficiency of ytterbium at 980 nm. The schematic diagram of the spectrum measurement system is given in Figure 2.1.3. The cuvette holder in the middle has four light ports, which offer two perpendicular light paths for excitation light and fluorescence measurement. The excitation light coming from SMA fibre is collimated by a SMA Fibre Adapter mounted to the left light port of cuvette holder. The collimated excitation light passes through the cuvette and is collected by a power meter mounted on the right light port of cuvette holder for power measurement. The emission light from samples is coupled into two spectrometers simultaneously by two optical lenses installed on the front and back light port of cuvette. The entire emission spectrum is directly recorded by software connected with two spectrometers. Finally, a cuvette holder cover is used to protect the cuvette from stray and ambient light that may enter from the top of cuvette holder.

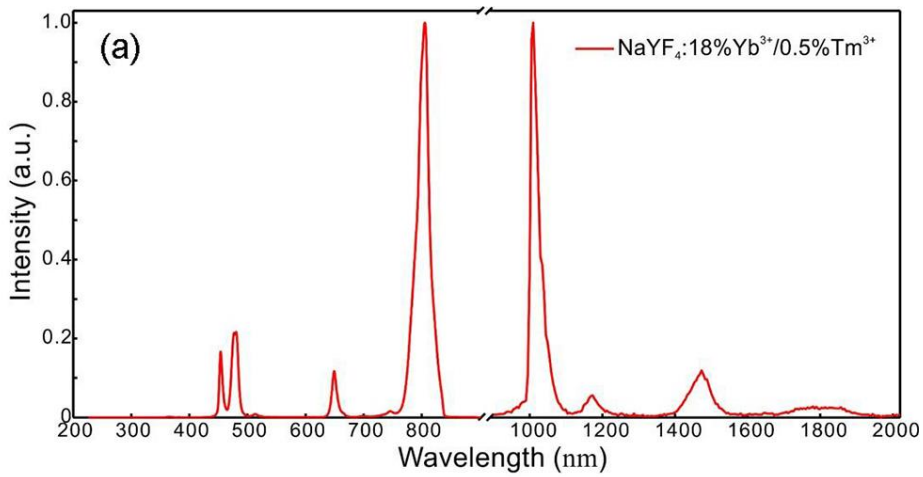

Figure 2.1.1. Efficient visible upconversion and near-infrared downshifting in $NaYF_4$:Yb:Er @$NaLuF_4$ core−shell nanocrystals, reprinted with free permission based on Creative Commons license© (2017) Nature communications [61] (http://creativecommons.org/licenses/by/4.0/).

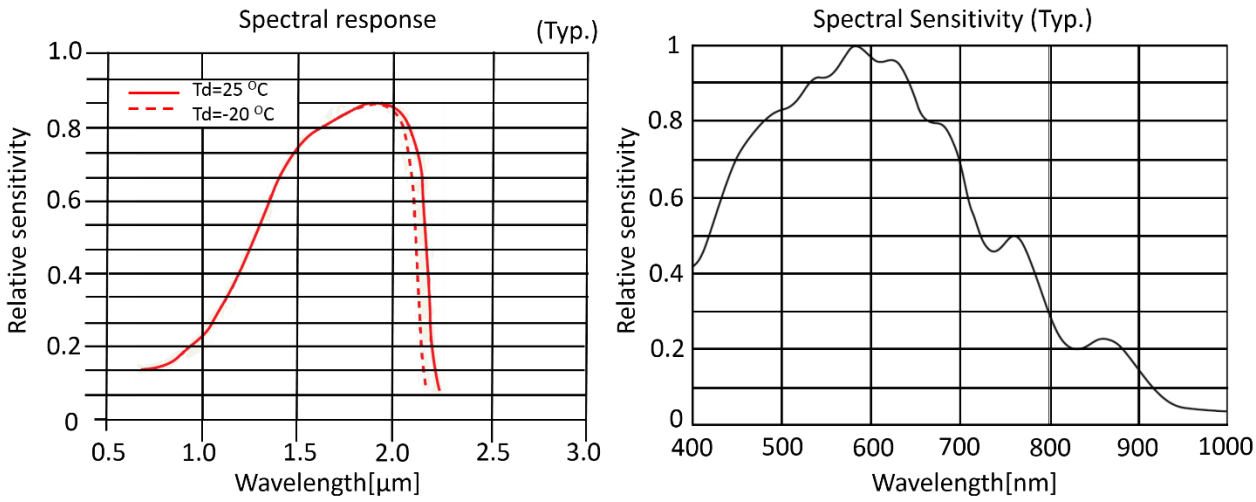

Figure 2.1.2. The quantum efficiency (electrons/photon) and wavelength range of (Left) InGaAs linear image sensor G9206-512W. Copyright© Hmamatsu Photonics Inc. (https://www.hamamatsu.com/resources/pdf/ssd/g9211-256s_etc_kmir1011e.pdf), and (Right) Silicon CCD linear sensor ILX511B. Copyright© Sony Inc. (https://oceanoptics.com/wp-content/uploads/SONY-ILX511B.pdf).

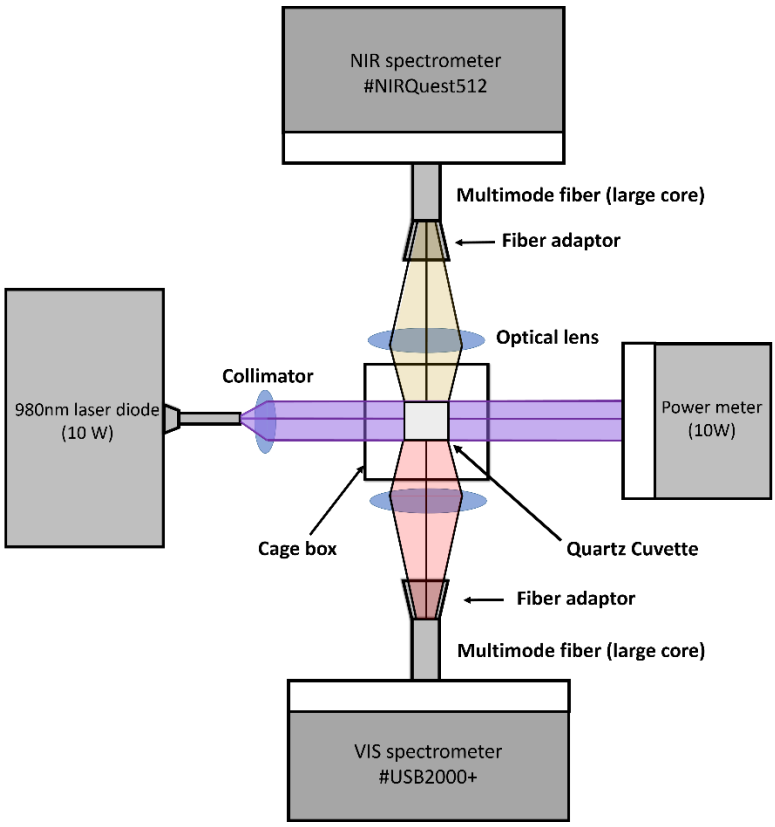

Figure 2.1.3. Schematic of the optical system structure.

2.1.2 Optical design

1. Choose optical lens for emission collection

In optics, the critical requirement for achieving high signal collection efficiency is the numerical aperture (*NA*) of the lens. As shown the Figure 2.1.4, the *NA* is related to the acceptance angle θ, which indicates the size of a cone of light that can be collected by the lens. Both *NA* and acceptance angle are linked to the refractive index *n* via:

$$NA = n * \sin(\theta) \tag{2.1}$$

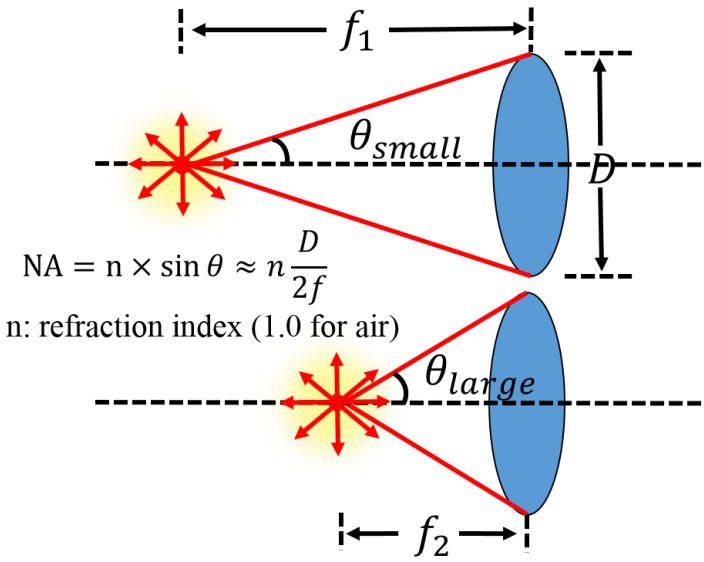

Figure 2.1.4. The comparison of light collection ability between small and large *NA* lens.

The luminescence from samples can be considered a point source, which diffuses in all directions. Therefore, choosing a collimating lens with high *NA* can increase the emission collection efficiency. We found the Thorlabs ACL12708U made by B270 has the highest *NA* up to 0.78 on the market.

The transmission rate of an optical component or its coating film is another key factor that affects the emission collection efficiency. A high Transmission rate permits the passage of incident light with little or none being absorbed by the lens in the process. Figure 2.1.5 compares the transmission rate of four typical materials: Fused Silica, N-BK7, S-LAH64 and B270 at different wavelengths. N-BK7 and B270 have the good transmission rate from 300 nm to 2200 nm, which is suitable for the emission spectrum of lanthanide doped nanocrystals. Therefore, ACL12708U is chosen to couple emission light into the fibre.

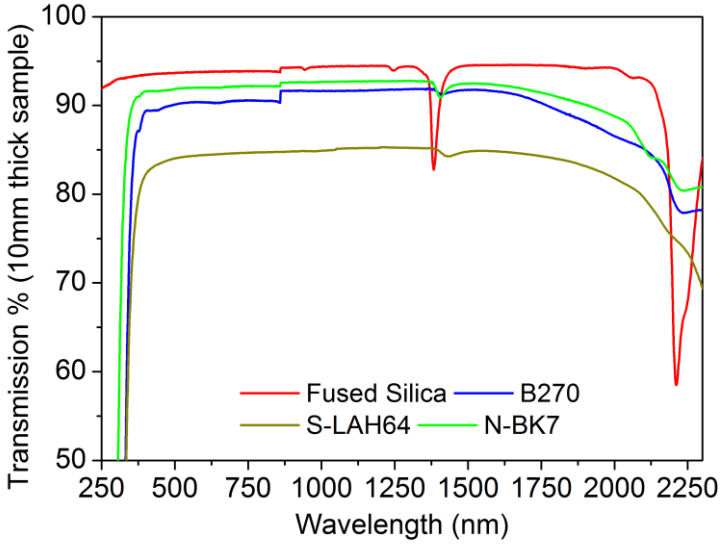

Figure 2.1.5. Transmission of four typical materials. Copyright© Thorlabs Inc. (https://www.thorlabs.com/newgrouppage9.cfm?objectgroup_id=6973).

Further, to satisfy the highest emission collection efficiency, the optical fibre also has to be optimum. The collection efficiency of optical fibre is determined by two factors: wavelength range and core diameter. The wavelength range of optical fibre must be broader than the emission spectrum of 300 nm to 1800 nm. The core diameter depends on the collimating lens and the Distance between Lens and Emission Targets (DLET). Theoretically, the DLET is shorter, the collection efficiency is higher. In practical, the distance between luminescence source and collimating lens is limited to an adjustable minimum distance 17.72 mm shown in Figure 2.1.6. Then, an optical simulation is run on Zemax OpticStudio to calculate the optimal distance between collimating lens and optical fibre using this minimum distance. In the simulation, the luminescence from samples can be considered a point source P and the initial distance between P and the collimating lens is 17.72 mm (shown in Figure 2.1.7). The simulation result shows that the position of minimum RMS (root-mean-square) spot is at 7.22 mm from the back surface of the lens. The incoherent irradiance in Figure 2.1.7 shows that the size of RMS spot is 0.86 mm, but more than 95% of light is concentrated within yellow and red area that is an area within 0.52 mm diameter. Therefore, the core diameter must be larger than 0.52 mm to ensure most emission light is coupled into the fibre and also should be smaller than 0.86mm, in order to remove the unwanted multiple-order energy peaks and pass only the central maximum of the diffraction pattern. Finally, two multimode SMA fibres with 0.6 mm core diameter are determined: QP600-2-SR for UV/Visible from 300 nm-1100 nm and QP600-2-VIS-NIR for Visible /NIR from 400 nm-2100 nm.

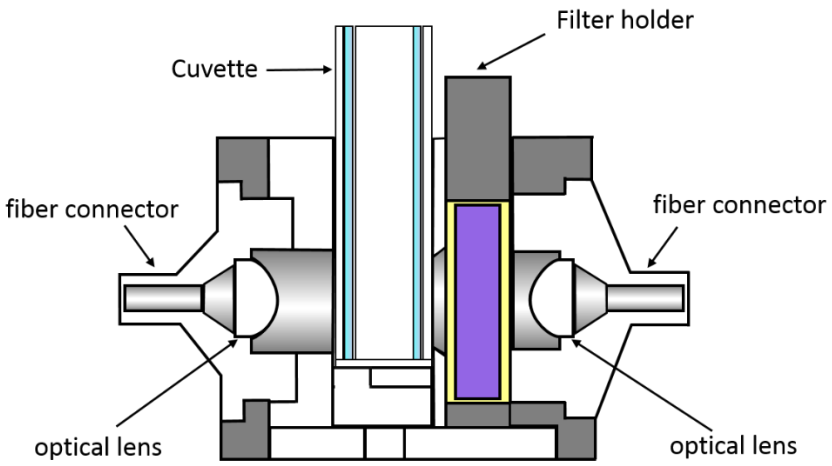

Figure 2.1.6. The mechanical design of the cuvette holder

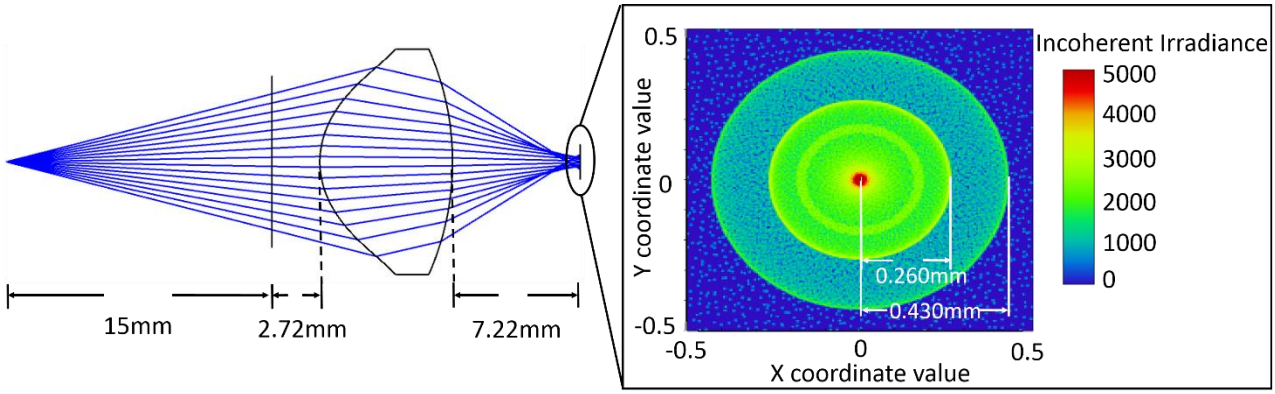

Figure 2.1.7. (Left) The diagram of the optical layout and (Right) corresponding incoherent irradiance result at focusing plane.

2.2 System calibration

Accurate quantification of the luminescence intensity for lanthanide doped nanocrystals requites calibration of two spectrometers because two spectrometers are designed for measuring different wavelength ranges. Figure 2.2.1 shows the structure and working principle of two spectrometers. When emission light enters the spectrometer, it passes a bandpass filter to restrict the transmission band to a certain wavelength range. The light then touches an aspheric mirror to become collimated beam and is reflected toward the diffraction grating. The diffraction grating is used to split the collimated beam to a group of wavelengths with spatial resolution (spectrum). Finally, the concave spherical mirror focuses the spectrum on the detector plane. The displayed wavelength range and intensity can be configured by adjusting the scale and exposure time.

Since the optical elements such as filter, grating, mirror, and detector are made of different materials in Custom USB2000+ and NIRQuest512. Their intensity response will not be at the same level despite the intensity response of a single spectrometer has been calibrated. Therefore, two spectrometers still need the calibration before capturing the data. In our calibration procedure, we calibrate the two spectrometers based on black-box testing method. The excitation light is measured by two spectrometers simultaneously and the intensity response from two spectrometers are compared to obtain the intensity coefficient.

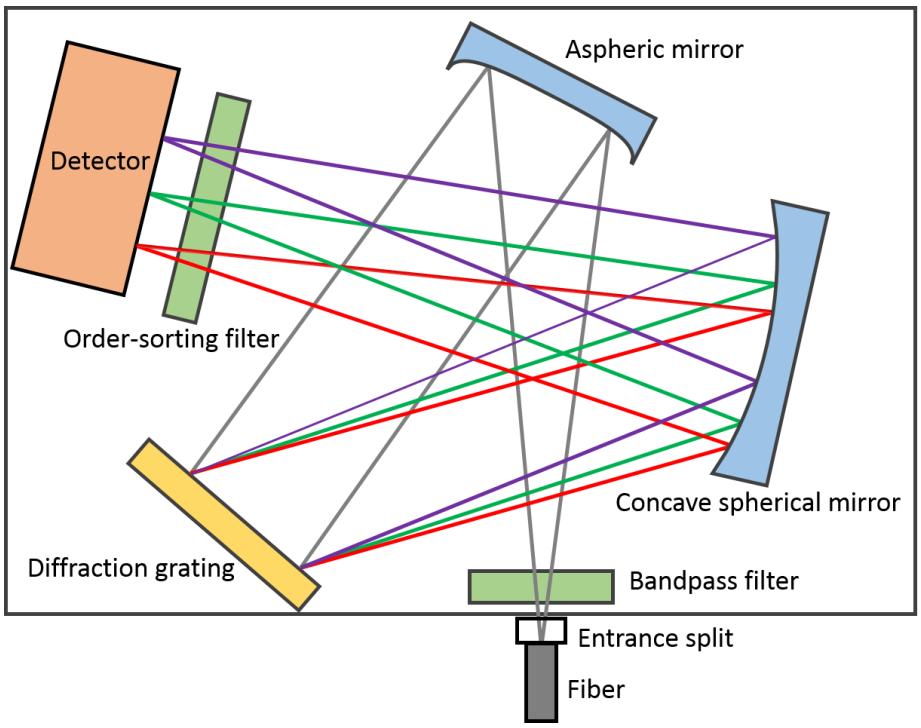

Figure 2.2.1. Schematic of spectrometer inside structure

2.2.1 Calibration method

The detection range of USB2000+ and NIRQuest512 is 300 nm to 1100 nm and 900 nm to 2200 nm, respectively. The wavelength of excitation laser diode is 980 nm, which is within the overlapping range (900 nm to 1100 nm). Therefore, it can be applied to this calibration. The wavelength of 980 nm laser diode is measured by USB2000+ and NIRQuest512 respectively using the same integrated time (250ms) under different power conditions, such as 600mW, 800mW and 1000mW. The measurement data is recorded in the computer by OceanView Software. Then, the data is analysed by Gaussian fitting method to get three groups of spectrum curves. Lastly, three ratios are calculated by comparing the maximum intensity of spectrum curves in three groups. The coefficient between two spectrometers is the average of these three ratios.

2.2.2 Calibration result

The Figure 2.2.2 (A, B and C) shows the results of measured spectra and fitted Gauss curves under three different power conditions: 600mW, 800mW and 1000mW using the same integrated time. Three ratios under three different power outputs are 1.318, 1.271, and 1.303, respectively, as shown in Figure 2.2.2 (D). Therefore, the final intensity coefficient for two spectrometers is the average of these three ratios 1.297.

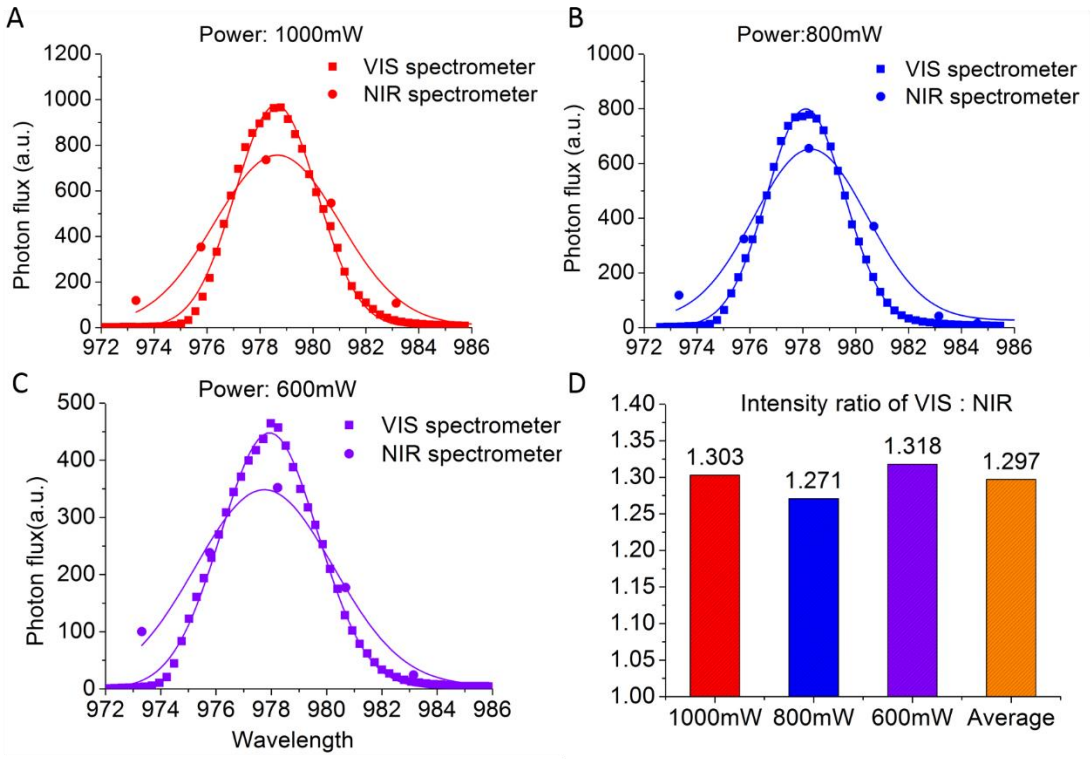

Figure 2.2.2. The diagram of measured spectra and fitted Gauss curves.

2.3 Experimental section

In this section, a valid experiment protocol is proposed, which includes two parts: 1) sample preparation, and 2) data acquisition. This experiment protocol not only contains all the steps that guide me to collect data, also includes notices that help me reduce experimental error, such as sample contamination.

2.3.1 Sample preparation and preservation

In our experiment, firstly, all the samples are configured in the same concentration 10mg/ml and frozen in the plastic tube below -5℃. The lanthanide nanocrystals that are monodisperse in

cyclohexane may expand and corrode the plastic tube at room temperature. Secondly, before injecting samples into the cuvette, the cuvette should be checked to make sure it is clean, in order to avoid the contamination by previous residues. Thirdly, all samples are used with the same volume 300µl for measurement. After one sample is injected in the cuvette, the cuvette should be sealed by plastic films because of two reasons: 1) Cyclohexane is very volatile, 2) the thermal effect of NIR excitation source is serious. Fourthly, due to the fact that plastic firm could be corroded by evaporated cyclohexane, it is prohibited to use near-infrared excitation source to illuminate the samples for a long time.

2.3.2 Data acquisition

1. Excitation power adjustment

During the experiment, the sample is excited by two excitation power range: first excitation power range is from 0W to 2W, and second excitation power range is from 2W to 8W. In the first excitation power range, the sample is measured every 100mW. In the second excitation power range, the excitation power step changes to 500mW. Therefore, there are 34 test points from 0W to 8W. The reason for doing in this way is because the sample has dramatic emission intensity increase when excitation power starts to rise in the beginning. The small steps for excitation intensity adjustment will help find the detail of this trend. Before measuring the spectrum, the excitation power should be adjusted and measured by the power meter in the absence of cuvette to prevent the light reflection from the surfaces of the cuvette. After the excitation intensity is recorded, the cuvette can be put into the cube box to measure the spectrum data.

2. Record the spectrum by optimized integration time

The lanthanide-doped nanocrystals have multiple emission bands because of a large number of energy transitions between discontinuous energy levels in lanthanide ions. For each test point (one excitation power), the integration time is regarded as optimal when the intensity of lowest emission peak exceeds the threshold (the ratio of background noise to the intensity of lowest emission peak is less than 0.1) to distinguish from background noise as well as the intensity of highest emission peak doesn’t exceed spectrometer’s detection limitation. If the condition is satisfied, the spectrum and its integration time are recorded. The lowest emission peak and the highest emission peak of each sample are summarized in Table 2.1 (by test):

Table 2.1. Min. and Max. Emission band in spectra of different nanoparticles

Sample Type	Min. Emission peak	Max. emission peak
$NaYF_4$:18%Yb:2%Er	525 nm	545 nm
$NaYF_4$:20%Yb:0.5%Tm	1472 nm	800 nm
$NaYF_4$:20%Yb:4%Tm	362 nm	800 nm
$NaYF_4$:20%Yb:0.5%Tm, 2%Gd	1472 nm	800 nm

3. Separate special emission peak from other emission peaks for measurement

It is found that some emission peaks have extremely different emission efficiency with others, the intensity of these emission peaks should be measured separately. For example, when 4% Tm^{3+} doped nanoparticles are excited, the intensity of the strongest emission peak 800 nm is at least 30 times larger than the weakest emission peak 362 nm. When I try to measure the weakest emission peak, the 800 nm emission intensity in USB2000+ is always saturated. Therefore, the entire luminescence spectrum cannot be captured by a single integration time. The same situation also happens to the NIR range, the intensity of downconversion emission peaks (wavelength>1000 nm) for both Tm^{3+} and Er^{3+} doped nanoparticles are usually smaller than upconversion emission peaks (wavelength<900 nm). To collect downconversion emission peaks with enough intensity, the integration time is set up to a few seconds, which is much longer than the integration time set up for upconversion data (microseconds).

4. Create the spectra by unifying integration time.

The whole spectrum is finally categorized to (1) upconversion emission peaks except 800 nm, (2) 800 nm emission peak, and (3) downconversion emission peaks. Each section measures the spectrum using their own integration time. Finally, all the emission peaks are integrated to a complete spectrum using identical integration time, and the intensity of downconversion emission peaks should multiply the intensity coefficient that is calculated in section 2.2.

3

Probing the competition between photoluminescence pathways in lanthanide-doped nanoparticles

This chapter examines the detailed photon conversion process in typical photoluminescent lanthanide nanoparticles doped with Yb as sensitizers and either Er or Tm as activators. The energy level diagrams of trivalent lanthanide ions are introduced first, along with the principle to be used for interpreting the correspondent spectroscopy results. These are then applied to the obtained power-dependent emission spectra of $NaYF_4$:Yb:Er and $NaYF_4$:Yb:Tm nanoparticles, highlighting potential competition pathways yielding upconversion and downconversion emission.

3.1 Energy transitions in lanthanide-doped nanoparticles.

It is well-known that trivalent lanthanide ions (Ln^{3+}) behave like isolated atoms, because they share the electron configuration of

$$1s^2\ 2s^2\ 2p^6\ 3s^2\ 3p^6\ 3d^{10}\ 4s^2\ 4p^6\ 4d^{10}\ 4f^n\ 5s^2\ 5p^6$$

Their low-lying energy states stem from different orbitals of the partially filled 4f subshell, which is shielded from the external electromagnetic fields by the full 5s and 5p subshells. As a result, the energy levels of Ln^{3+} are nearly independent of the host material. Their energy-level diagram, traditionally called the Dieke diagram, is shown in Figure 3.1.1.

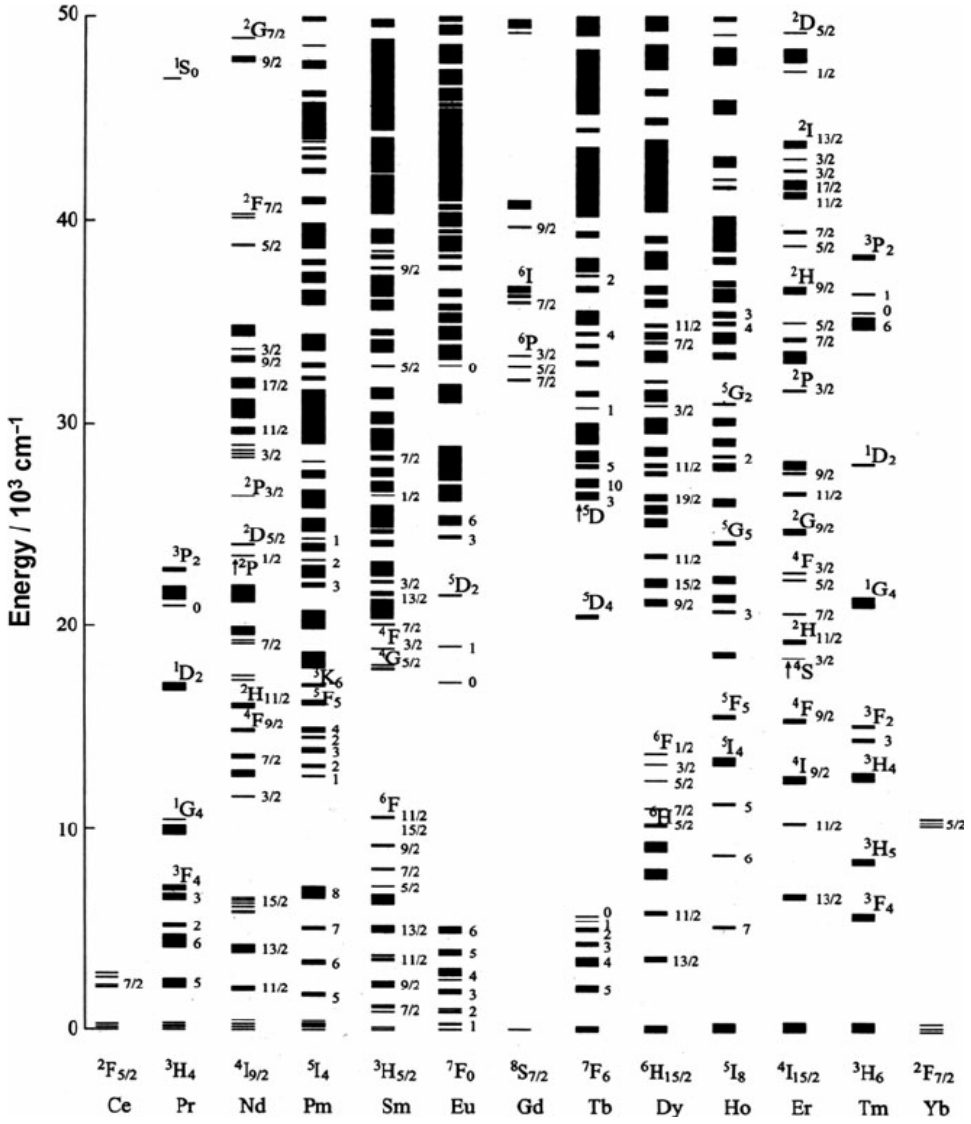

Figure 3.1.1. Energy-level diagram of trivalent lanthanide ions with $4f^n$ configurations, reprinted with permission from [62], Copyright (1989) AIP Publishing.

The actual values for many of these energy levels can be found from the NIST Atomic Spectra Database (https://physics.nist.gov/PhysRefData/ASD/levels_form.html) as well as in some classical literature [62-64]. It should be noted that, although the influence of host material is small, shifts of several hundred cm^{-1} may still be found for the same levels in different lattices.

Among the trivalent lanthanide ions, in this thesis I focus on Er^{3+} and Tm^{3+} as activators, which can be effectively sensitized by Yb^{3+} co-doped in host nanocrystals such as $NaYF_4$. The nanoparticles were synthesized by Dr. Xianlin Zheng and Dr. Liuen Liang from our group. According to the literature [65], the doping concentration of Yb^{3+} ions is maintained at 18~20% to offer optimum sensitization efficiency, whereas the doping concentration of Er^{3+} or Tm^{3+} ions is initially kept low

for this chapter. This help exclude complex Er-Er or Tm-Tm cross-relaxation pathways among their multiple energy levels so that the most basic photon conversion pathways can be clearly illustrated.

The experimental and analytical procedures to interpret the energy transitions in lanthanide-doped nanoparticles are as follows:

1) To measure the emission spectra for the nanoparticles using the setup and protocol described in Chapter 2.

2) To assign the observed emission peak to the energy transition among the energy levels, by correlating the emission peak to the energy gap.

3) In the case that more than one energy transfer pathways yield the emission peak, to assess the dominant energy transfer pathways based on the power-dependent data.

4) To discuss the relation among energy distribution of main emission peaks.

3.2 Yb^{3+}/Er^{3+} co-doped nanoparticles

3.2.1 Correlating emission spectrum to possible energy transitions

The $NaYF_4$:18%Yb:2%Er nanoparticles used here have a uniform size around 28 nm, as shown in the transmission electron microscopy (TEM) image (Figure 3.2.1). The emission spectrum is captured under 980 nm laser excitation with increasing intensity from 10 to 60 W/cm^2. Four major emission peaks are observed, including 525 nm, 540 nm and 655 nm upconversion luminescence and 1525 nm downconversion luminescence (Figure 3.2.2).

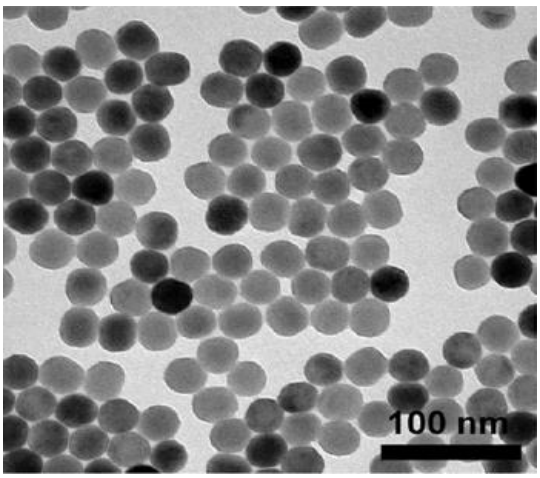

Figure 3.2.1. TEM image of $NaYF_4$:Yb:Er nanocrystals, the Yb and Er doping concentration are 18mol% and 2mol%, respectively. The nanocrystals have average size around 28 nm.

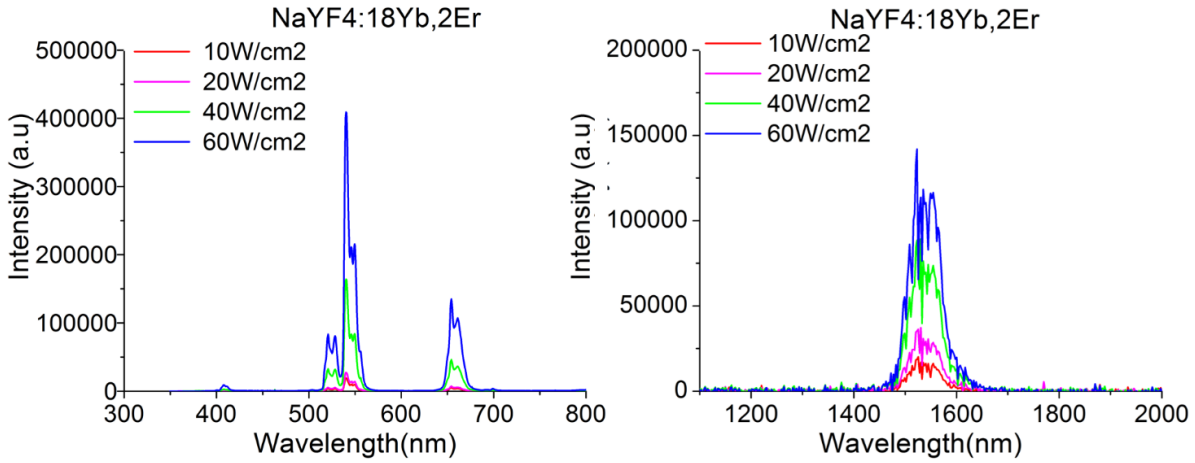

Figure 3.2.2. (Left) UV-NIR spectrum and (Right) SWIR spectrum of $NaYF_4$:18%Yb:2%Er under 980 nm laser, exposure time: 6s.

As we know, the wavelength (λ) can be transformed to the wavenumber (ν), which corresponds to the energy that lanthanide ions releases (or absorbs) when it transits between a high energy level and a low energy level. The relationship between the wavelength (in nm) and the wavenumber (in cm^{-1}) is:

$$\nu = 10^7/\lambda \qquad (3.1)$$

By searching for two energy levels separated by the corresponding wavenumber, we can identify possible energy transition that gives rise to the luminescence. The trivalent lanthanide ion has energy level with diverse bandwidth due to the different number of sub-energy levels included (shown in Figure 3.1.1), therefore complicated energy transitions occurred between energy levels will broaden emission peaks. We have calculated a list of wavenumbers (3 significant digits) corresponding to the four major emission peaks for Er^{3+} ions by equation 3.1 in Table 3.1. The energy level scheme for Er^{3+} is shown in Figure 3.2.3 [63].

Table 3.1. Emission peaks and their transferred wavenumbers.

Emission peaks (nm)	Wavenumber (cm^{-1})
525	$1.90 * 10^3$
545	$1.83 * 10^3$
655	$1.52 * 10^3$
1525	$0.65 * 10^3$

Assuming the 525 nm emission ends up on the ground level $^4I_{15/2}$, the initial level of transition is likely to be $^2H_{11/2}$, which yields 19010.8 cm^{-1} for free Er^{3+}, 19117 cm^{-1} for Er^{3+} in LaF_3, and 19036

cm^{-1} for Er^{3+} in $Lacl_3$. Similarly, we can obtain the energy transition between energy levels corresponding to the remaining three emission peaks (Table 3.2).

Energy-level assignments for Er^{3+}									
S'L'J'	Er^{3+} (free ion)			Er^{3+} in LaF_3[b]			Er^{3+} in $LaCl_3$[c]		
	E_{exptl} (cm^{-1})	E_{cale}[d] (cm^{-1})	ΔE (cm^{-1})	E_{exptl} (cm^{-1})	E_{cale}[d] (cm^{-1})	ΔE (cm^{-1})	E_{exptl} (cm^{-1})	E_{cale}[d] (cm^{-1})	ΔE (cm^{-1})
$^4I_{15/2}$	0	96	-96	217	232	-15	108	130	-22
$^4I_{13/2}$	6485.9	6567	-81	6697	6732	-35	6589	6630	-41
$^4I_{11/2}$	10123.6	10140	-16	10340	10335	5	10219	10226	-7
$^4I_{9/2}$	12345.5	12294	61	12567	12504	63	12438	12377	61
$^4F_{9/2}$	15182.9	15202	-19	15452	15432	20	15283	15260	23
$^4S_{3/2}$	18299.6	18445	-145	18570	18696	-126	19398	18536	-138
$(^2H,^4G)_{11/2}$	19010.8	19096	-85	19334	19398	-64	19144	19181	-37
$^4F_{7/2}$	20494.1	20391	103	20709	20652	57	20515	20449	66
$^4F_{5/2}$	22181.8	22014	168	22378	22305	73	22174	22097	77
$^4F_{3/2}$	22453.9	22368	86	22711	22645	66	22516	22449	67
$(^2G,^4F)_{9/2}$	24475.2	24367	108	24744	24644	100	24565	24471	94
$^4G_{11/2}$	26376.9	26348	29	26585	26680	-95	26367	26397	-30
$^4G_{9/2}$	27319.2	27333	-14	27629	27693	-64	27327	27358	-31
$^4K_{15/2}$	27584.9	27597	-12	...	27857	...	27605	27643	-38
$^4G_{7/2}$	27825.0	27843	-18	28298	28176	122	27987	27909	78
$(^2P,^4D)_{3/2}$	31414.4	31496	-82	317718	31844	-126	31497	31625	-128
$^4K_{13/2}$	32972.2	32862	110	33139	33145	-6	32963	32927	36
...	...	...	...	...	...	...	...	...	...
	rms Deviation		141			84			84

Figure 3.2.3. The energy level scheme of Er^{3+} including study of Er^{3+}(free-ion), Er^{3+} in LaF_3, and Er^{3+} in $Lacl_3$, reprinted with permission from [63], Copyright (1968) AIP Publishing.

Table 3.2. Typical lanthanide activator Er^{3+} with its emission peaks and corresponding energy transitions

Emission peaks	Energy transition	Reason
525 nm ($1.90 * 10^3\ cm^{-1}$)	$^2H_{11/2} \rightarrow {}^2I_{15/2}$	19010.8 cm^{-1} for free Er^{3+}, 19117 cm^{-1} for Er^{3+} in LaF_3, and 19036 cm^{-1} for Er^{3+} in $Lacl_3$
545 nm ($1.83 * 10^3\ cm^{-1}$)	$^4S_{3/2} \rightarrow {}^4I_{15/2}$	18299.6 cm^{-1} for free Er^{3+} , 18353 cm^{-1} for Er^{3+} in LaF_3, and 18290 cm^{-1} for Er^{3+} in $Lacl_3$
655 nm ($1.52 * 10^3\ cm^{-1}$)	$^4F_{9/2} \rightarrow {}^4I_{15/2}$	15182.9 cm^{-1} for free Er^{3+}, 15235 cm^{-1} for Er^{3+} in LaF_3, and 15175 cm^{-1} for Er^{3+} in $Lacl_3$
1525 nm ($0.65 * 10^3\ cm^{-1}$)	$^4I_{13/2} \rightarrow {}^4I_{15/2}$	6485.9 cm^{-1} for free Er^{3+}, 6480 cm^{-1} for Er^{3+} in LaF_3, and 6481 cm^{-1} for Er^{3+} in $Lacl_3$

3.2.2 Relationship between luminescence intensity and n-photon absorption process

The luminescence intensity of lanthanide-doped nanoparticles is power-dependent, which involves competitions between (1) ground-state absorption (GSA), (2) subsequent energy-transfer upconversion (ETU), (3) excited-state absorption (ESA), and (4) depletion by luminescence. Figure 3.2.4 shows a simple model for a four-step energy transition process. The slope (*n*) in the logarithm-logarithm plot of emission intensity to excitation intensity is typically used to indicate the number of absorption photons required to populate the excitation state [66, 67].

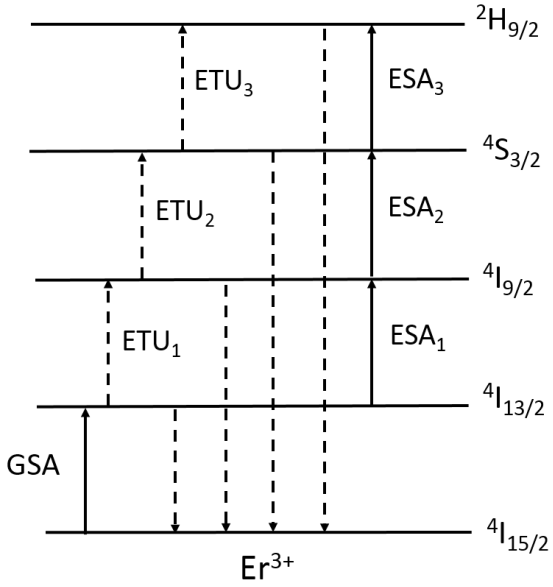

Figure 3.2.4. Simple model for four-step energy transition process.

According to a detailed model by Pollnau et al., there are different situations for the slope (*n*) depending on the excitation pathway, upconversion rate, and predominant decay pathway. This is explained as follows [68]:

The pump rate R_i of an energy transition from state i can be written as:

$$R_i \approx \frac{\lambda_p}{hc\pi w_p^2} P\sigma_i N_i = \rho_p \sigma_i N_i \qquad (3.2)$$

with λ_p the pump wavelength, w_p the pump radius, h Planck's constant, c the vacuum speed of light and P the incident pump power. ρ_p is pump constant which equals to $\frac{\lambda_p}{hc\pi w_p^2} P$, σ_i is the absorption cross section from state i and N_i is its population density. Each state i have lifetime τ_i and decay with rate constants $A_i = \tau_i^{-1}$.

If the upconversion is achieved solely by ETU process with a corresponding parameter W_i, the pump rate equation for excited-state population densities N_i is:

$$N_i = \prod_{j=2,\dots i}\left[W_{j-1}A_j^{-1}\right]\left(\rho_p\sigma_0N_0\right)^i,\ i = 1,\dots.n \tag{3.3}$$

$$N_i = \prod_{j=2,\dots i}\left[W_{j-1}A_j^{-1}\right]\prod_{k=2,\dots n-1}\left[A_k^{i/n}\right]\times\prod_{l=2,\dots n-1}\left[W_l^{-i/n}\right]\left(\rho_p\sigma_0N_0\right)^{i/n}, i = 1,\dots.n \tag{3.4}$$

$$\begin{cases} N_i = 0.5W_1^{0.5}W_i^{-1}\left(\rho_p\sigma_0N_0\right)^{0.5}, i = 1,\dots n-1 \\ N_n = 0.25A_n^{-1}\rho_p\sigma_0N_0 \end{cases} \tag{3.5}$$

(3.3) for small upconversion rate with predominant decay to both next low-lying state and ground state;
(3.4) for large upconversion rate with predominant decay to next low-lying state;
(3.5) for large upconversion rate with predominant decay to ground state.
If the upconversion is achieved solely by ESA process, the pump rate equations for excited-state population densities N_i become:

$$N_i = \prod_{j=1,\dots i}\left[\sigma_{j-1}\right]N_0\prod_{j=1,\dots i}\left[A_j^{-1}\right]\rho_p^i\ ,\ i = 1,\dots.n \tag{3.6}$$

$$\begin{cases} N_i = (\sigma_0/\sigma_i)N_0,\ \ i = 1,\dots,n-1 \\ N_n = A_n^{-1}\rho_p\sigma_0N_0. \end{cases} \tag{3.7}$$

(3.6) for small upconversion rate with predominant decay to both next low-lying state and ground state as well as large upconversion rate with predominant decay to next low-lying state;
(3.7) for large upconversion rate with predominant decay to ground state.

From Equations 3.3 to 3.7, it can be seen that the luminescence intensity for an *n*-photon absorption process is proportional to the *n*-th power of the excitation power (P^n) in the limit of infinitely small population rate, while the luminescence intensity is proportional to the excitation power (P^1) for the upper state and less than P^1 for the intermediate states in the limit of infinitely large population rate. Therefore, the luminescence intensity of an energy transition by sequential absorption of *n* photons has a dependence of P^β on excitation power *P* with $\beta<n$ [68]. It should be noted that, in real situations where the nanoparticles have defective surfaces and/or interiors, the luminescence intensity may deviates from this power-dependent rule.

3.2.3 Interpreting dominant upconversion pathways

To find out the dominant energy transfer pathways that support the energy transitions in Er-doped nanoparticles, the logarithm-logarithm plot of emission intensity to excitation intensity for upconversion emission peaks is drawn in Figure 3.2.5. The slopes (*n*) for 525 nm, 545 nm, and 655 nm are 1.64, 1.88, and 1.78, respectively, when excitation intensity is less than 11 W/cm^2. As the excitation intensity increases from 11 W/cm^2 to 60 W/cm^2, the slopes (*n*) become 2.42, 2.44, and 2.49, respectively (Table 3.3).

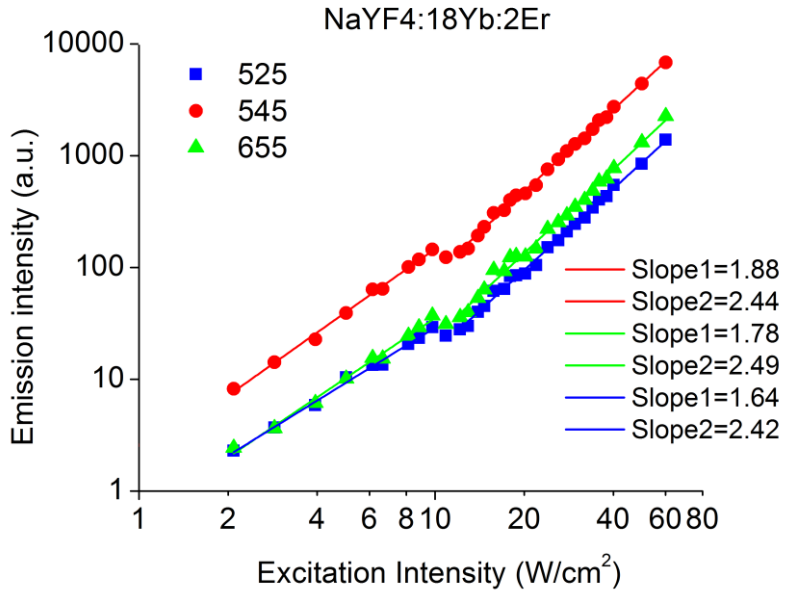

Figure 3.2.5. Logarithm-logarithm plot of emission intensity to excitation intensity for 525 nm, 545 nm, and 655 nm, exposure time: 500ms.

Table 3.3. Experimental slopes (*n*) for different emission peaks in $NaYF_4$:18%Yb:2%Er nanoparticles under 980 nm excitation

Emission peaks	Transition	n (1 – 11 W/cm^2)	n (11 – 60 W/cm^2)
525 nm	$^2H_{11/2} \rightarrow {}^4I_{15/2}$	1.64	2.42
545 nm	$^4S_{3/2} \rightarrow {}^4I_{15/2}$	1.88	2.44
655 nm	$^4F_{9/2} \rightarrow {}^4I_{15/2}$	1.78	2.49

In the low excitation power state (1-11 W/cm^2), the slopes between 1 and 2 indicate energy transition $^2H_{11/2} \rightarrow {}^4I_{15/2}$, $^4S_{3/2} \rightarrow {}^4I_{15/2}$, $^4F_{9/2} \rightarrow {}^4I_{15/2}$ are all populated by two-photon process from Yb^{3+} to Tm^{3+}. The slopes are approximate values corresponding to the number of photons involved in the process (e.g. slopes of 1.57 and 1.76 both indicate two-photon emission process) [66, 69-72]. It is known that

a single 980 nm excitation photon has energy of 10204 cm^{-1}, the energy transition $^2H_{11/2} \rightarrow {}^2I_{15/2}$ (19010 cm^{-1}), $^4S_{3/2} \rightarrow {}^4I_{15/2}$(18299 cm^{-1}), $^4S_{3/2} \rightarrow {}^4I_{15/2}$ (15182 cm^{-1}) have less energy than 2 excitation photons (20408 cm^{-1}), therefore can be populated by two-photon process, which matches the conclusion received from slope in power-dependent luminescence diagram.

The possible dominant energy transfer pathways in the low excitation power state are highlighted in Figure 3.2.6A. The Er^{3+} ions at ground state $^4I_{15/2}$ absorb two photons from Yb^{3+} and jump to the excited state $^4F_{7/2}$ because of the very close energy. The excited state $^4F_{7/2}$ then populates lower states $^2H_{11/2}$ and $^4S_{3/2}$ for 525 nm and 545 nm emission through non-radiative relaxation. For the energy state $^4F_{9/2}$, there are two pathways that can populate it:

1. the Er^{3+} ions at ground state $^4I_{15/2}$ first absorb one photon and jump to the excited state $^4I_{11/2}$ (≈10123 cm^{-1}). After subsequent non-radiative relaxation from $^4I_{11/2}$ (≈10123 cm^{-1}) to $^4I_{13/2}$ (≈6486 cm^{-1}), the Er^{3+} ions at excited state $^4I_{13/2}$ absorb another photon and jump to the excited state $^4F_{9/2}$ (≈15183 cm^{-1}), which is the contributor to 655 nm emission;

2. the Er^{3+} ions at ground state $^4I_{15/2}$ absorb two photons and jump to the excited state $^4F_{7/2}$, then drop to the lower state $^4F_{9/2}$ through non-radiative relaxation $^4F_{7/2} \rightarrow {}^4F_{9/2}$. Both two pathways are possible.

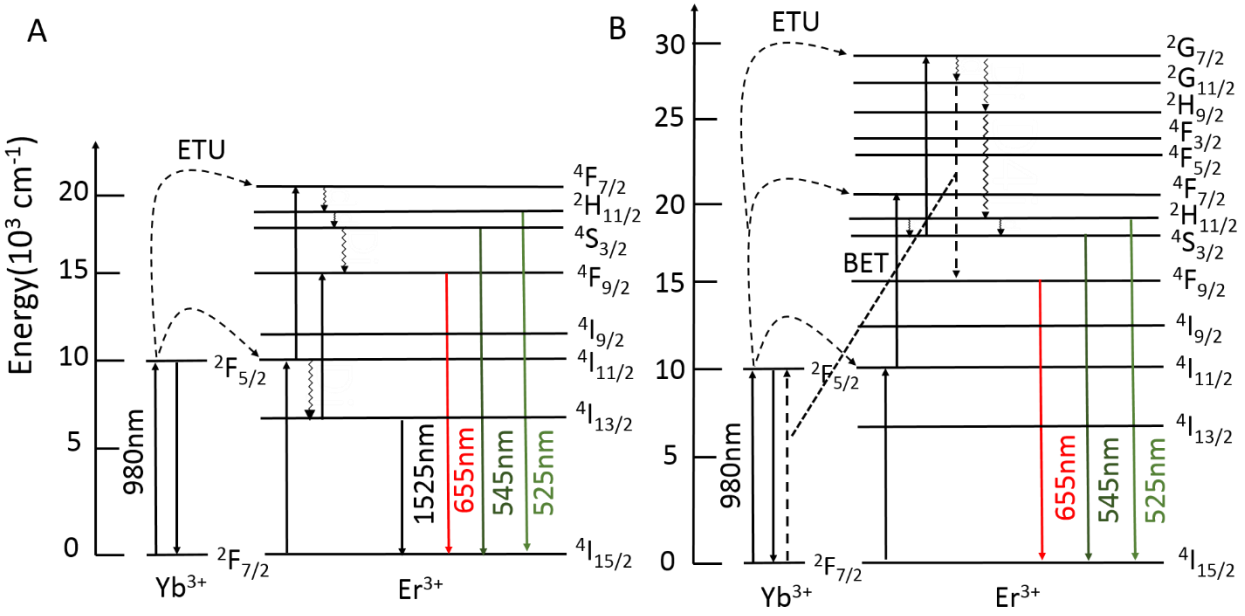

Figure 3.2.6. Energy transfer scheme of Yb^{3+} to Er^{3+}, with arrows indicating the dominant population pathways at (A) low excitation intensity and (B) high excitation intensity, respectively. ETU: energy transfer upconversion, and BET: back energy transfer.

In the high excitation power state (11-60 W/cm^2), the slopes between 2 and 3 indicate the population of energy states $^2H_{11/2}$, $^4S_{3/2}$, $^4F_{9/2}$ come from three-photon process. Since three-photon process is much more complicated than two-photon process, I can only present the basic dominant energy transfer pathways in Figure 3.2.6B.

The Er^{3+} ions at ground state $^4I_{15/2}$ absorb three photons and jump to the energy state $^4G_{7/2}$ (≈27285 cm^{-1}), For emission peaks 525 nm (19048 cm^{-1}) and 545 nm (18349 cm^{-1}), however, there isn't energy transition between energy level $^4G_{7/2}$ and another energy level that matches the energy of 525 nm or 545 nm. Therefore, the excited state $^2H_{11/2}$, $^4S_{3/2}$ are directly populated by $^4G_{7/2}$ through non-radiative relaxation process. For emission peak 655 nm, the excited state $^4G_{11/2}$ (≈26377 cm^{-1}) is populated by $^4G_{7/2}$ firstly, then a back-energy transfer happens between $^4G_{11/2}$ of Er^{3+} ions and $^2F_{7/2}$ of Yb^{3+} ions ($^4G_{11/2} \rightarrow {}^4F_{9/2}$(≈11194 cm^{-1}), $^2F_{7/2} \rightarrow {}^2F_{5/2}$(≈10204 cm^{-1})) so that the energy state $^4F_{9/2}$ is finally populated for 655 nm emission. It is noticed that the intensities of all upconversion emission peaks are suddenly reduced at the excitation intensity of 11 W/cm^2 (Figure 3.2.5). The reason for this happen may be the temporary depletion of Tm^{3+} ions at intermediate energy states $^4I_{11/2}$ and $^4F_{7/2}$ because of the enhancement of three-photon process.

3.2.4 Interpreting downconversion pathways

Under the logarithm-logarithm plot of emission intensity to excitation intensity for the 1525 nm peak (Figure 3.2.7A), linear fitting yields a Pearson correlation coefficient (*r*) of 98.97%, indicating the data points do not correspond to a perfect line (for which *r* should be larger than 99%). Therefore, I calculated the slopes (*n*) in two excitation ranges which are separated by the excitation power node 11 W/cm^2. The values of both first slope (1.14, with *r* of 99.54%) and second slope (1.37, with *r* of 99.54%) are between 1 and 2, indicating the population of energy state $^4I_{13/2}$ not only stems from one-photon process but also involves two-photon process. Since the photon absorption and emission processes are power-dependent, higher excitation power will lead to a stronger 2-photon absorption process to populate the energy transition for 1525 nm peak. Therefore, the second slope becomes larger than the first slope. The possible dominant energy transfer pathways are highlighted in Figure 3.2.7B.

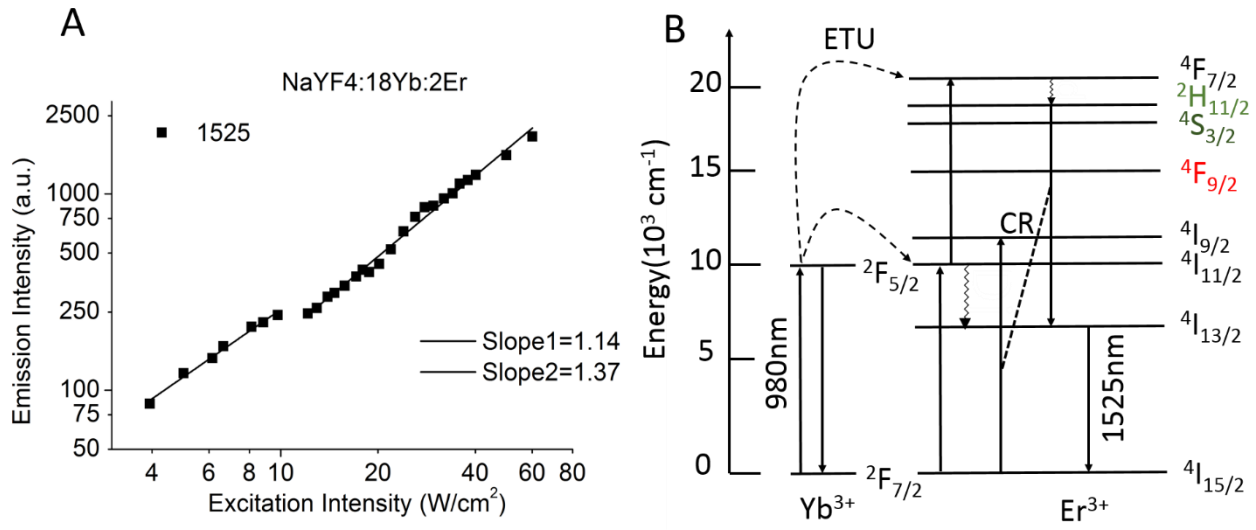

Figure 3.2.7. (A) Logarithm-logarithm plot of emission intensity to excitation intensity for 1525 nm, exposure time: 500ms. (B) Energy transfer scheme of Yb^{3+}-Er^{3+} interactions, with arrows indicating the dominant population pathways for downcoversion process. ETU: energy transfer upconversion. CR: cross-relaxation

For the one-photon process, the Er^{3+} ions at ground state $^4I_{15/2}$ absorb one photon and jump to the energy state $^4I_{11/2}$, which populates the energy state $^4I_{13/2}$ for 1525 nm emission by non-radiate relaxation process. For the two-photon process, the Er^{3+} ions at ground state $^4I_{15/2}$ absorb two photons and jump to the energy state $^4F_{7/2}$, then relax to $^2H_{11/2}$. An additional cross-relaxation between energy state $^4I_{15/2}$ and $^2H_{11/2}$ ($^4I_{15/2} \rightarrow {}^4I_{9/2}$, $^2H_{11/2} \rightarrow {}^4I_{13/2}$) happens so that the energy transition $^4I_{13/2} \rightarrow {}^4I_{15/2}$ are populated.

3.2.5 Competition between up- and down-conversion pathways

Since the emission efficiency of upconversion and downconversion luminescence is governed by the competition between their respective population and depopulation rates from Yb^{3+} and intermediate states of Er^{3+}, we need to explore the dynamic energy distribution of each emission peak as the excitation power changes from low to high. Here I define the energy distribution is the contribution of integral photon flux of single emission peak $I(\lambda)$ to overall integral photon flux $I(\lambda_{all})$. The integral photon flux is calculated by the sum of emission photon flux in the specific emission peak, and the overall photon flux is the sum of photon flux of all the emission peaks (Figure 3.2.8). The ranges of emission peaks are summarized in Table 3.4.

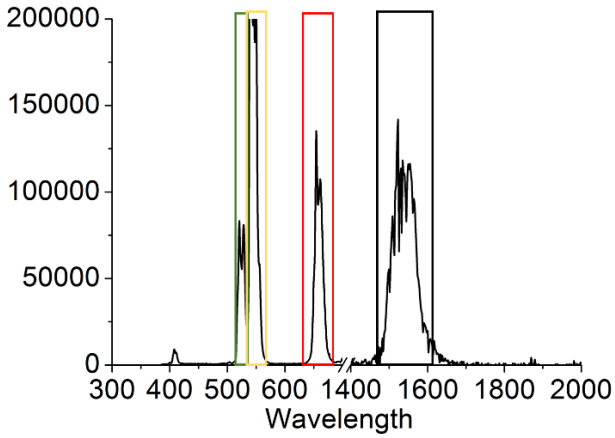

Figure 3.2.8. The integration of emission photon flux in specific range of emission peak.

Table 3.4. The emission peaks and their corresponding ranges.

Emission peak	Peak range
525 nm	517 nm – 532 nm
545 nm	536 nm – 558 nm
655 nm	649 nm – 669 nm
1525 nm	1487 nm – 1600 nm

As excitation intensity changes from 0 to 60 W/cm^2, the energy distribution of 1525 nm peak is decreasing from 55.1% to 16.8%, while the energy distribution of 525 nm, 545 nm, and 655 nm peaks are increasing from 6.6%, 28.1%, 11.6%, to 10.2%, 49.6%, and 22%, respectively (Figure 3.2.9). It indicates that the intensity of 1525 nm is inversely proportional to the excitation power whereas the intensities of 525 nm, 545 nm, and 655 nm are proportional to the excitation power.

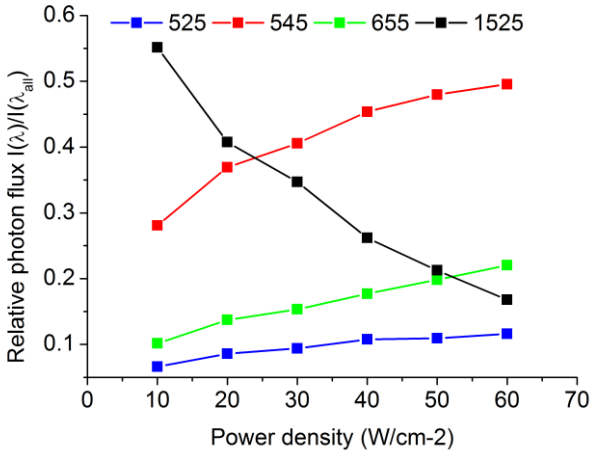

Figure 3.2.9. Contribution of the integral intensities of different emission peaks I(λ) to the overall integral intensity I(λ_{all}), exposure time: 6s.

In conclusion, the $NaYF_4$:18%Yb:2%Er has ability to emit emission peaks 525 nm, 545 nm, 655 nm, and 1525 nm. The corresponding energy transitions have been summarized in Table 1, and the energy transfer pathways that support energy transitions have been analysed in Figure 3.2.5, Figure 3.2.6, and Figure 3.2.7. Moreover, the energy distribution of emission peaks is also analysed in Figure 3.2.9. The whole result shows that high excitation power will help increase the intensity of all the emission peaks. However, the emission efficiency of 1525 nm decreases as excitation intensity becomes large.

3.3 Yb^{3+}/Tm^{3+} co-doped nanoparticles

3.3.1 Correlating emission spectra to possible energy transitions

The sample of $NaYF_4$:20%Yb:0.5%Tm is used here to explore the energy transitions in Yb^{3+}/Tm^{3+} co-doped nanoparticles. It has a uniform size around 40 nm, as shown in the transmission electron microscopy (TEM) image (Figure 3.3.1).

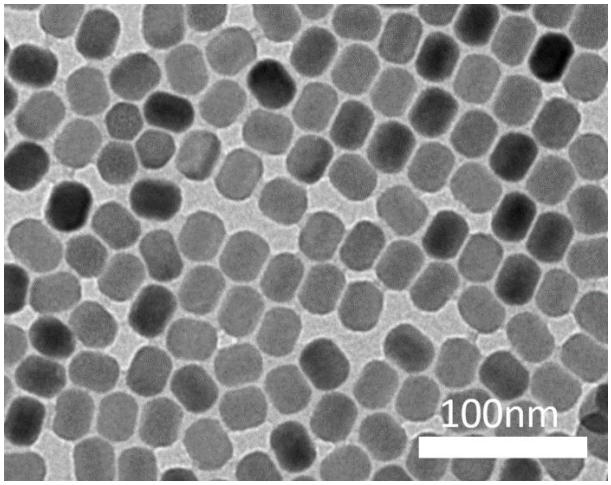

Figure 3.3.1. TEM image of $NaYF_4$:Yb:Tm nanocrystals, the Yb and Tm doping concentration are 20 mol% and 0.5 mol%, respectively. The nanocrystals have average size around 40 nm. Scale bar, 100 nm.

The emission spectrum under 980 nm excitation with intensity from 10 to 80 W/cm^2 is shown in Figure 3.3.2. It shows that Tm^{3+} ions have more emission peaks than Er^{3+} ions. To be specific, the $NaYF_4$:20%Yb:0.5%Tm has five primary upconversion peaks 361 nm, 450 nm, 477 nm, 646 nm, 800 nm with significant emission intensity as well as three secondary upconversion peaks 693 nm, 724 nm, 741 nm with weak emission intensity. Meanwhile, the downconversion peak 1472 nm is also found in the spectrum. To simplify the analysis, I focus on five primary upconversion peaks and one

downconversion peak. Three secondary upconversion peaks are ignored due to the complex energy transfer pathways behind them.

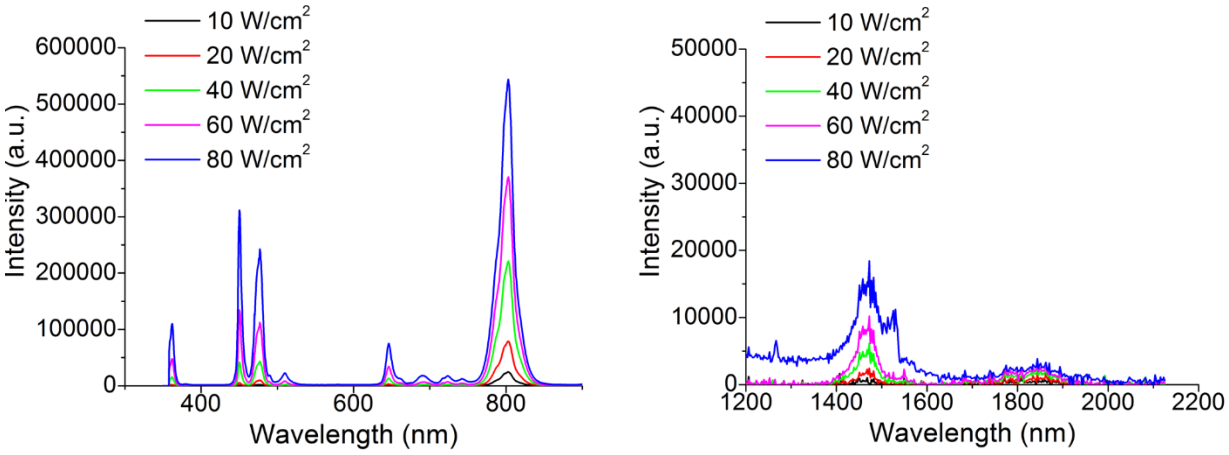

Figure 3.3.2. (Left) UV-NIR spectrum and (Right) SWIR spectrum of $NaYF_4$:20%Yb:0.5%Tm under 980 nm laser, exposure time: 6s.

Like what we did for Er^{3+}, the emission peaks are first transferred to the corresponding wavenumbers (Table 3.5).

Table 3.5. Emission peaks and their corresponding wavenumbers

Emission peaks	Wavenumbers
361 nm	$2.77*10^3$ cm^{-1}
450 nm	$2.22*10^3$ cm^{-1}
477 nm	$2.10*10^3$ cm^{-1}
646 nm	$1.55*10^3$ cm^{-1}
800 nm	$1.25*10^3$ cm^{-1}
1472 nm	$6.80*10^3$ cm^{-1}

The two energy levels that have the same energy with observed emission peak are found out by searching the atom spectra database (NIST) or classic literature. (A list of energy assignment for Tm^{3+} is displayed in Figure 3.3.3). Therefore, we obtain the energy transitions corresponding to all the observed emission peaks (Table 3.6). Except for these observed emission peaks, the energy transition $^3P_2 \rightarrow {}^3H_6$ creates another emission peak around 260 nm through fifth-photon process, which is outside the measurable range of our system but has been discussed in the literature [72]. It is mentioned that the discrepancy between the energy of $^3P_2 \rightarrow {}^3H_6$ transition and the total energy of five photons is due to non-radiative relaxation.

Energy-level assignments and matrix elements of U(λ) for Tm^{3+} (aq).									
S'L'J'	$Tm(C_2H_5SO_4)\cdot 9H_2O$[a]			Tm^{3+} (aq.)					
	E_{exptl} (cm^{-1})	E_{cale}[d] (cm^{-1})	ΔE (cm^{-1})	E_{exptl} (cm^{-1})	E_{cale}[d] (cm^{-1})	ΔE (cm^{-1})	$U(2)^o$	$U(4)^o$	$U(6)^o$
$^3H_6$	170	141	29	170	202	-32	...	...	...
$^3F_4$	5846	5787	59	5900	5811	89	0.5375	0.7261	0.2382
$^3H_5$	8250	8326	-76	8400	8390	10	0.1074	0.2314	0.6383
$^3H_4$	12665	12673	-8	12700	12720	-20	0.2373	0.1090	0.5947
$^3F_3$	14464	14514	-50	14500	14510	-10	0	0.3164	0.8411
$^3F_2$	15192	15112	80	15100	15116	-16	0	~0	0.2581
$^1G_4$	21300	21306	-6	21350	21374	-24	0.0483	0.0748	0.0125
$^1D_2$	27916	28014	-98	28000	28032	-32	0	0.3156	0.0928
$^1I_6$	34870	34851	19	34900	34886	14	0.0106	0.0388	0.0134
$^3P_0$	35444	35641	-197	35500	35637	-137	0	0	0.0756
$^3P_1$	36461	36295	82	38250	38193	57	0	0	0.1239
$^3P_2$	38257	38175	82	38250	38193	57	0	0.2645	0.0223
$^1S_0$	...	79720	...	...	79592	...	0	0	0.0002
rms Deviation			143			94			84

Figure 3.3.3. The energy level scheme of Tm^{3+} including study of $Tm^{3+}(C_2H_5S0_4)_3 \cdot 9H_20)$, Tm^{3+}(aquo ion), reprinted with permission from [63] Copyright (1968) AIP Publishing.

Table 3.6. Typical lanthanide activator Tm^{3+} with its emission peaks and energy transitions

Emission peaks	Energy transition	Reason
361 nm ($2.77*10^3$ cm^{-1})	$^1D_2 \rightarrow {}^3H_6$	27746 cm^{-1} for $Tm^{3+}(C_2H_5S0_4)_3 \cdot 9H_20)$, and 27830 cm^{-1} for Tm^{3+}(aq)
450 nm ($2.22*10^3$ cm^{-1})	$^1D_2 \rightarrow {}^3F_4$	22070 cm^{-1} for $Tm^{3+}(C_2H_5S0_4)_3 \cdot 9H_20)$, and 22100 cm^{-1} for Tm^{3+}(aq)
477 nm ($2.10*10^3$ cm^{-1})	$^1G_4 \rightarrow {}^3H_6$	21130 cm^{-1} for $Tm^{3+}(C_2H_5S0_4)_3 \cdot 9H_20)$, and 21180 cm^{-1} for Tm^{3+}(aq)
646 nm ($1.55*10^3$ cm^{-1})	$^1G_4 \rightarrow {}^3F_4$	15454 cm^{-1} for $Tm^{3+}(C_2H_5S0_4)_3 \cdot 9H_20)$, and 15450 cm^{-1} for Tm^{3+}(aq)
800 nm ($1.25*10^3$ cm^{-1})	$^3H_4 \rightarrow {}^3H_6$	12495 cm^{-1} for $Tm^{3+}(C_2H_5S0_4)_3 \cdot 9H_20)$, and 12530 cm^{-1} for Tm^{3+}(aq)
1472 nm ($6.80*10^3$ cm^{-1})	$^3H_4 \rightarrow {}^3F_4$	6819 cm^{-1} for $Tm^{3+}(C_2H_5S0_4)_3 \cdot 9H_20)$, and 6800 cm^{-1} for Tm^{3+}(aq)

3.3.2 Interpreting dominant upconversion pathways

To investigate the energy transfer pathways that underpin luminescence emission, we again draw the logarithm-logarithm plot of emission intensity to excitation intensity (Figure 3.3.4). It shows that the luminescence of 800 nm, 646 nm, 477 nm have monomial (i.e. linear in log-log plot) relationship with excitation intensity in the range of 1 to 20 W/cm^2, which is confirmed by the result of Pearson's *r* (99.85% for 800 nm, 99.93% for 477 nm, 99.83% for 646 nm). On the other hand, the luminescence of 361 nm and 450 nm is nonlinear with excitation intensity at low range (1 to 3 W/cm^2). By fitting the luminescence of 361 nm and 450 nm in this region, we obtain slopes of 0.83 and 1.35, which are significantly small in comparison to those (i.e. 4-photon) corresponding to the predominant energy transfer pathways. This is likely due to the fact that the signal strength is very low compared to the noise background, which yield inaccurate fitting results. Therefore, this region is excluded from the curve fitting analysis. As excitation intensity increases from 3 to 11 W/cm^2, the relationship between the luminescence of 361 nm and 450 nm and excitation intensity become linear in the log-log plot. Finally, the slopes for all emission peaks change again when excitation intensity becomes large than 11 W/cm^2. The detailed slope variations are summarized in Table 3.7, the photon absorption and energy transfer processes are explained in the following paragraphs.

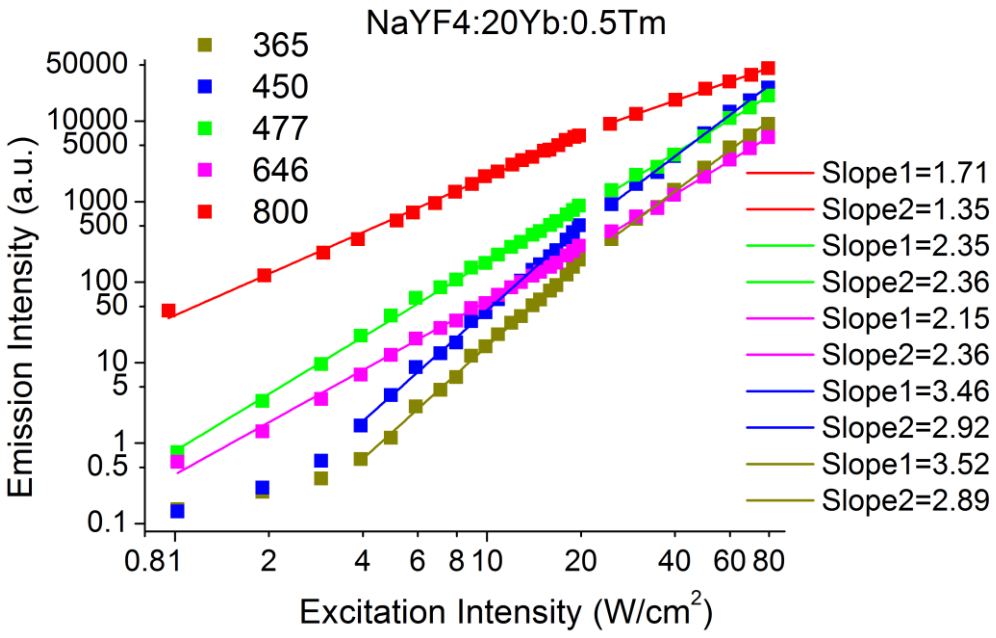

Figure 3.3.4. Logarithm-logarithm plot of emission intensity to excitation intensity for 525 nm, 545 nm, and 655 nm, exposure time: 500 ms.

Table 3.7. Experimental slopes (*n*) for different emission in $NaYF_4$:20%Yb:0.5%Tm nanoparticles under 980 nm excitation

Emission peaks	Energy Transition	n(3 – 11 W/cm^2)	n(11 – 60 W/cm^2)
361 nm	$^1D_2 \rightarrow {}^3H_6$	3.52	2.89
450 nm	$^1D_2 \rightarrow {}^3F_4$	3.46	2.92
477 nm	$^1G_4 \rightarrow {}^3H_6$	2.35	2.36
646 nm	$^1G_4 \rightarrow {}^3F_4$	2.15	2.36
800 nm	$^3H_4 \rightarrow {}^3H_6$	1.71	1.35

In Table 3.7, the slopes for 477 nm and 646 nm are between 2 and 3, indicating the population of energy state $^1G_4$ comes from 3-photon absorbing process. Similarly, the slopes for 800 nm indicate the 2-photon absorbing process for populating $^3H_4$. As for the population of energy state $^1D_2$, the energy gap (6616 cm^{-1}) between $^1D_2$ and $^1G_4$ doesn't match the energy of one photon transferred from Yb^{3+} to Tm^{3+}. Therefore, the cross-relaxation process between Tm^{3+} ions may alternatively play an important role in populating $^1D_2$ level. The possible dominant energy transfer pathways are explained below:

The Tm^{3+} ions at ground state absorb one photon energy and jump to energy level $^3F_4$, then jump to the energy state $^3H_4$ (12665 cm^{-1}) by absorbing second photon energy. The energy transition $^3H_4 \rightarrow {}^3H_6$, therefore, generates 800 nm emission. In addition, some Tm^{3+} ions at energy state $^3H_4$ will continuous to absorb third photon energy and jump to the energy state $^1G_4$ (21300 cm^{-1}). The energy transitions $^1G_4 \rightarrow {}^3F_4$ and $^1G_4 \rightarrow {}^3H_6$ generate 646 nm and 477 nm emission, respectively. The population of $^1D_2$ is completed by cross-relaxation processes. Two possible cross-relaxation processes may populate $^1D_2$: (1) $^3H_4 \rightarrow {}^1D_2$ (15251 cm^{-1}), $^1G_4 \rightarrow {}^3F_4$ (15454 cm^{-1}), and (2) $^1G_4 \rightarrow {}^1D_2$ (6616 cm^{-1}), $^3H_4 \rightarrow {}^3F_4$ (6819 cm^{-1}) [72]. The Tm^{3+} ions at energy state $^1G_4$ finally relax to the ground state $^3F_4$ and energy state $^3H_6$ to generate 450 nm and 361 nm emission, respectively. The detail photon transfer processes are displayed in Figure 3.3.5.

In the high excitation power state (11-60 W/cm^2), the slopes for 361 nm ($^1D_2 \rightarrow {}^3H_6$), 450 nm ($^1D_2 \rightarrow {}^3F_4$) and 800 nm ($^3H_4 \rightarrow {}^3H_6$) decrease apparently from 3.52, 3.46 and 1.71 to 2.89, 2.92 and 1.35, while the slopes for 477 nm ($^1G_4 \rightarrow {}^3H_6$), 646 nm ($^1G_4 \rightarrow {}^3F_4$) increase slightly from 2.35 and 2.15 to 2.36. The slope decreasing can be treated as the consequence of serious saturation of excitation

states $^1D_2$ and $^3H_4$. The intermediate energy state $^1G_4$ doesn't become saturated, indicating additional energy transfer process is consuming its population. Given a high doping concentration of Yb^{3+}, the back-energy transfer of $^1G_4$ (Tm^{3+}) + $^2F_{7/2}$ (Yb^{3+}) →$^3H_4$ (Tm^{3+}) + $^2F_{5/2}$ (Yb^{3+}) may be the main reason that leads the depopulation of $^1G_4$ [73] (Figure 3.3.5).

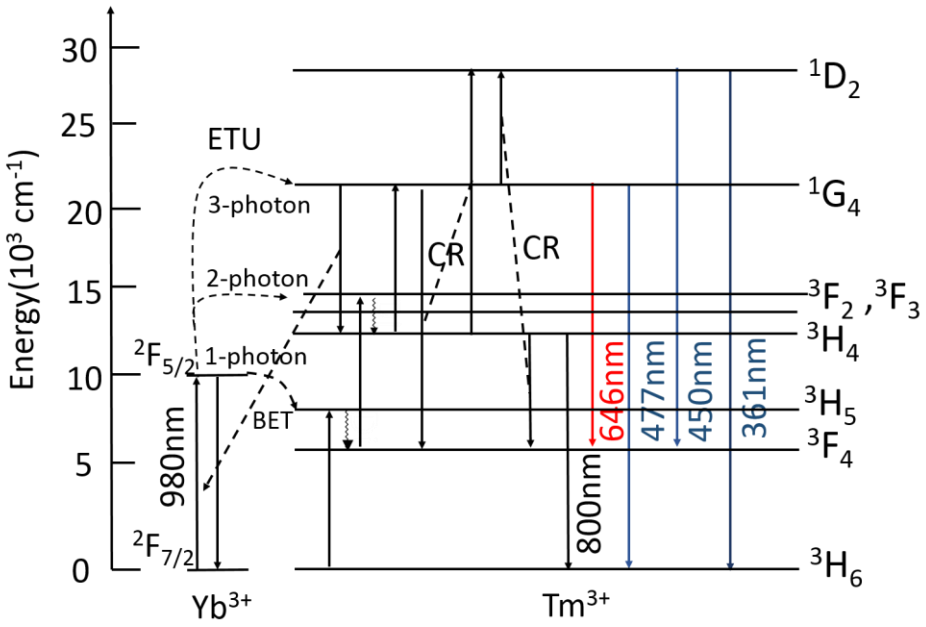

Figure 3.3.5. Energy scheme of Yb^{3+}-Tm^{3+} interactions, with arrows indicating the dominant population pathways. ETU: energy transfer upconversion, CR: cross-relaxation process.

3.3.3 Interpreting downconversion pathways

When turning to the logarithm-logarithm plot of emission intensity to excitation intensity for 1472 nm (Figure 3.3.6A), the emission at low excitation power is unstable due to its weak intensity. Therefore, the intensity data is collected under the excitation power from 20 to 70 W/cm^2.

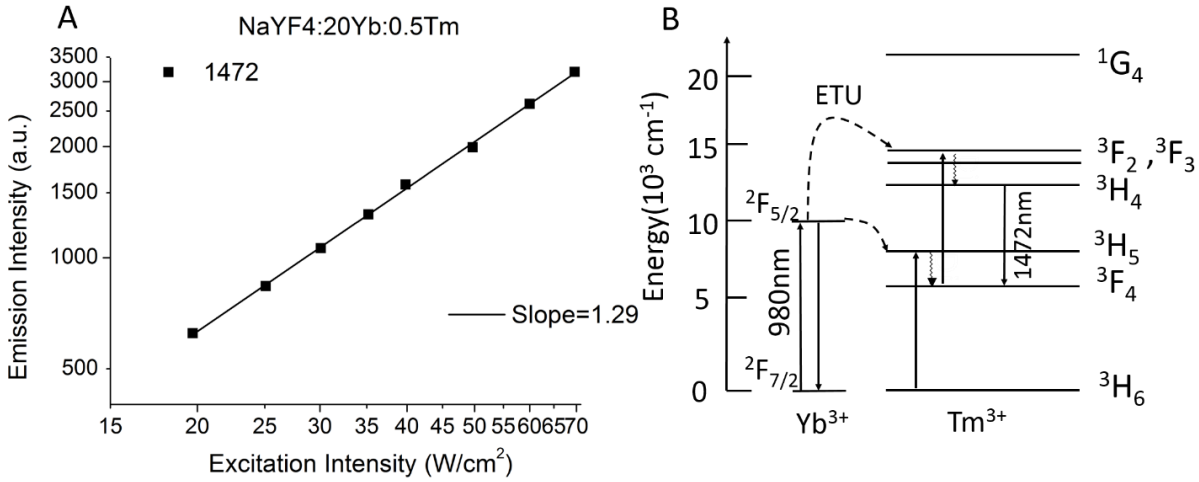

Figure 3.3.6. (A) Logarithm-logarithm plot of emission intensity to excitation intensity for 1472 nm, exposure time: 2s. (B) Energy transfer scheme of Yb^{3+}-Tm^{3+} interactions, with arrows indicating the dominant population pathways for downconversion process. ETU: energy transfer upconversion.

From Figure 3.3.6A, the slope value (1.29) indicates the population of energy transition $^3H_4 \rightarrow {}^3F_4$ comes from two-photon process. The detailed energy transfer pathways for populating $^3H_4$ are shown in Figure 3.3.6B. Instead of relaxing to ground state $^3H_6$ to generate 800 nm emission, the energy state $^3H_4$ relaxes to the lower state $^3F_4$ to emit luminescence of 1472 nm.

3.3.4 Competition between up- and down-conversion pathways

To discuss the dynamic energy distribution of emission peaks, the emission efficiency for special emission peak is defined as the ratio of the integral photon flux of a single emission peak I(λ) to the overall integral photon flux I(λ_{all}), which is the same with what we did in section 3.2.5. The ranges of emission peaks for photon flux integration are summarized in Table 3.8:

Table 3.8. The integration range of each emission peak.

Emission peak	Peak range
361 nm	358 nm – 367 nm
450 nm	445 nm – 460 nm
477 nm	465 nm – 486 nm
646 nm	641 nm – 653 nm
800 nm	769 nm – 832 nm
1472 nm	1393 nm – 1593 nm

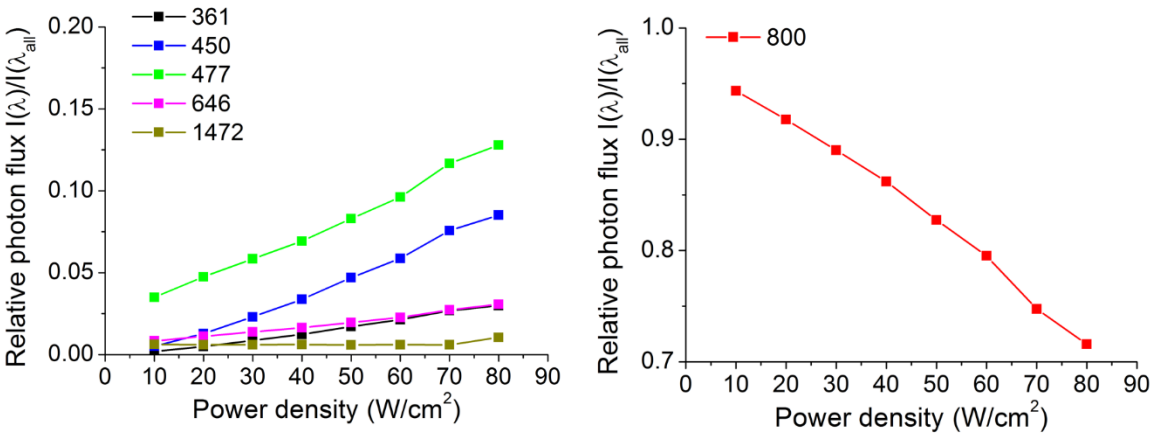

Figure 3.3.7. The ratio of the integral intensities of different emission peaks I(λ) to the overall integral intensity I(λ_{all}), exposure time: 6s.

According to the Figure 3.3.7, the 800 nm peak possesses nearly all the emission energy (94.4%) at low excitation intensity, other emission peaks 361 nm, 450 nm, 477 nm, 646 nm, 1472 nm only take up energy of 0.2%, 0.5%, 3.5%, 0.8%, 0.6%, respectively. However, as excitation intensity increases, the 800 nm peak reduces its proportion while the proportion of other emission peaks start to increase. At the excitation intensity of 80 W/cm^2, the proportion of 800 nm reduces to 71.6% and the proportion of 361 nm, 450 nm, 477 nm, 646 nm, 1472 nm increase to 3%, 8.5%, 12.8%, 3%, and 1%, respectively. In conclusion, the emission efficiency of 800 nm reduces, and the emission efficiency of other emission peaks increases as excitation power become large.

3.4 Remarks

In this chapter, I first measure the spectrum data of Yb^{3+}/Er^{3+}co-doped nanoparticles NaYF4:18%Yb:2%Er^{3+} and Yb^{3+}/Tm^{3+}co-doped nanoparticles NaYF4:20%Yb:0.5%Tm^{3+} under excitation intensity from 0-60 W/cm^2. Then I correlate the energy transitions to emission peaks based on the matching of their energy. To assess the potential energy transfer pathways, I measure the power-dependent emission intensity for each emission peak and give my speculation about energy transfer pathways according to the slope value. Finally, I calculate the dynamic energy distribution of emission peaks and give my conclusion about the emission efficiency variation as excitation power increases.

4

Exploring the influence of doping on the energy distribution in lanthanide nanoparticles

In this section, I conduct a preliminary investigation into the impact on the energy distribution when the doping concentration is varied or when a new dopant is added. The Yb/Tm co-doped system is used, since the Tm activators do not absorb the excitation light and do not transfer energy back to the Yb sensitizers (unlike Er in the Yb/Er system), thereby easing the analysis. Possible mechanisms underlying the spectroscopic changes are proposed, in an attempt to form some guidelines that may help improve the efficiency for specific emission wavelengths, especially for downconversion in the short-wavelength infrared region.

4.1 The effect of doping concentration

4.1.1 Comparison of emission spectra

As mentioned in section 3.3, the sample of $NaYF_4$:20%Yb:0.5%Tm with low Tm concentration has a very weak emission intensity of 1472 nm, which may be caused by the limited number of Tm^{3+} ions: the majority of Tm^{3+} ions are excited to a high state $^1G_4$ and $^1D_2$ to emit upconversion light (646 nm, 800 nm, etc.). Therefore, the high Tm concentration (4%) is selected to compare the variation on energy distribution. Figure 4.1.1 shows the spectrum from 0.5% and 4% Tm^{3+} doped nanoparticles on both upconversion band (Left) and downconversion band (Right). It shows that the intensity of upconversion peaks (361 nm, 450 nm, 477 nm, 646 nm) from 4% Tm^{3+} doped nanoparticles are almost negligible compared to that from 0.5% Tm^{3+} doped nanoparticles, indicating the non-existent of 3-photon and 4-photon absorption processes. From the decreased intensity of 800 nm and 1472 nm, we know the 2-photon absorption process also become weaker. Therefore, it concludes that most Tm^{3+} ions are undergoing one-photon process or even unexcited in 4% Tm^{3+} doped nanoparticles.

The emission of 1850 nm which suddenly appears but does not appear in 0.5% Tm^{3+} doped nanoparticles also help confirm the presumption because its energy transition $^3F_4 \rightarrow {}^3H_6$ mainly stems from one-photon process: $^3H_6 \rightarrow {}^3H_5 \rightarrow {}^3F_4$ where $^3H_5 \rightarrow {}^3F_4$ is the non-radiation relaxation (Figure 3.3.6).

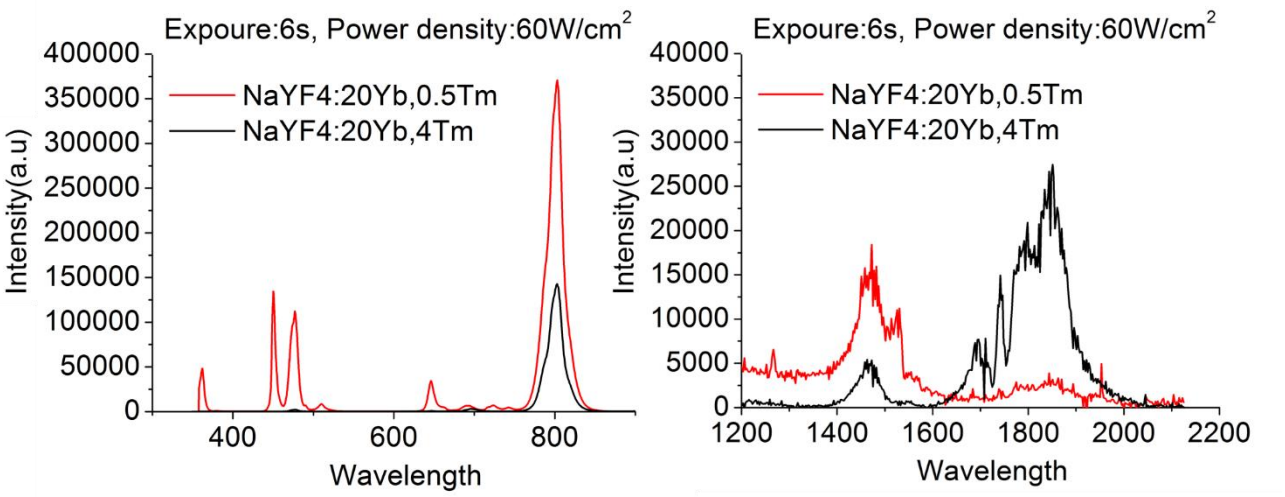

Figure 4.1.1. Comparison of UV-NIR spectrum (Left) and SWIR spectrum (Right) on 0.5%Tm^{3+} and 4% Tm^{3+} concentration (20% Yb^{3+}).

4.1.2 Additional pathways introduced by high Tm doping

The reason that most Tm^{3+} ions are undergoing one-photon process or unexcited can be explained in the following way:

As the concentration of Tm become larger, the ratio of Yb:Tm changes from 40:1 to 5:1. When the ratio of Yb:Tm is 40:1, excessive Yb^{3+} ions are "feeding" one Tm^{3+} ion at a time so that before Tm^{3+} ion relaxing to the ground, new photons are coming and absorbed by Tm^{3+} ion instantly. The Tm^{3+} ion continues to jump to higher energy levels. Therefore, there is no sufficient time for Tm^{3+} ion to execute one-photon luminescence process. However, as the ratio of Yb:Tm becomes 5:1, the number of Yb^{3+} ions that support single Tm^{3+} ion reduces dramatically. As a result, it takes longer time for Yb^{3+} ions to "feed" Tm^{3+} ion at the ground state. This slight "delay" gives excited Tm^{3+} ion enough time to relax to the ground state. Therefore, the one-photon process becomes stronger than the two-photon or three-photon process (illustrated in Figure 4.1.2).

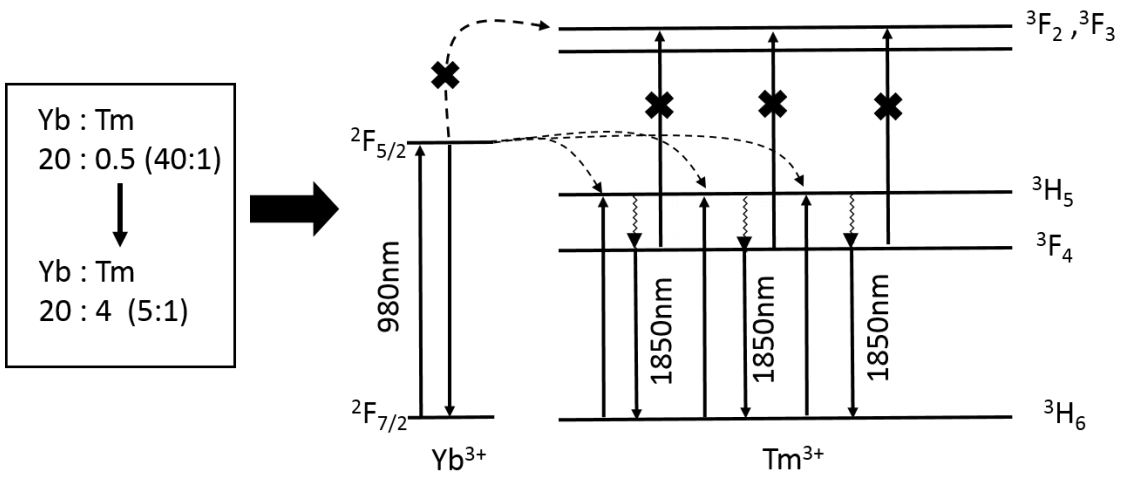

Figure 4.1.2. The new energy transfer scheme for high Tm doping nanoparticle (20% Yb^{3+}).

In addition, the high Tm doping concentration may induce additional energy transfer pathways that enhance the energy transition process of 1850 nm. Generally, the concentration of Tm increases, the opportunity of cross-relaxation among Tm^{3+} ions increases as well. As shown in Figure 4.1.3, the energy transition $^3H_4 \rightarrow ^3F_4$ which originally creates 1472 nm emission may transfer its energy to the ground state $^3H_6$ and pump Tm^{3+} ion to the energy state $^3F_4$ due to their similar energy gap: $^3H_4 \rightarrow ^3F_4$ (6819 $cm^{-1)}$ and $^3H_6 \rightarrow ^3F_4$ (5676 cm^{-1}). Because of the intensive cross-relaxation process in high Tm doping nanoparticle, the intensity of emission peak 1850 nm become lager and the intensity of 1472 nm becomes weaker, which is similar to what we see in the spectrum.

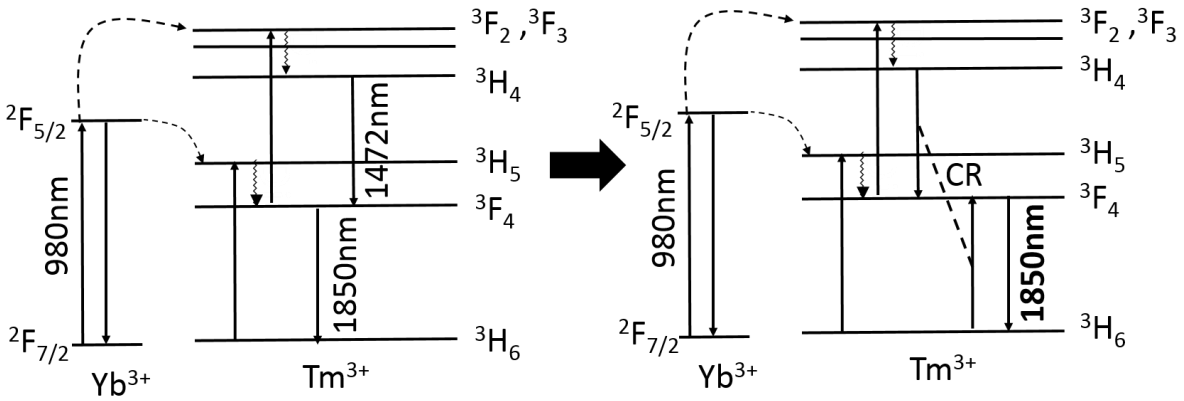

Figure 4.1.3. The change of energy transfer pathways induced by high Tm doping.

4.1.3 Influence on the energy distribution

Figure 4.1.4 (A, B) shows the variation of emission intensities as excitation power increases from 1 to 8W. From the figure, we know that the intensity of 800 nm increases much faster than other

emission peaks and all the emission peaks are continuously increasing their intensities at different speeds. Since most Tm^{3+} ions in 4% Tm^{3+} doped nanoparticle are only undergoing one- and two-photon processes at current excitation range, Figure 4.1.4 (C, D) compares the intensity ratio of 800 nm ($^3H_4 \rightarrow {}^3H_6$) to 1472 nm ($^3H_4 \rightarrow {}^3F_4$) and 1850 nm ($^3F_4 \rightarrow {}^3H_6$) for 4% and 0.5% doped nanoparticles, respectively. In Figure 4.1.4C, the intensity ratio of 800 nm to 1472 nm maintains a comparatively small variation for 0.5% Tm^{3+} doped nanoparticle under different power densities, indicating there may be a stable ratio between energy transitions from same excitation state ($^3H_4$) to different lower states ($^3H_6$ and $^3F_4$). However, this stable ratio cannot be applied for 4% Tm^{3+} doped nanoparticle at insufficient excitation power. In Figure 4.1.4D, since the dominant upconversion process for 4% Tm^{3+} doped nanoparticle is one-photon process, the intensity ratio of 800 nm to 1850 nm is much smaller than that from 0.5% Tm^{3+} doped nanoparticle. Therefore, increasing the concentration of Tm dopant as well as dominating the upconversion process by only one-photon process through low power excitation or cross-relaxation process like $^3H_4 \rightarrow {}^3F_4$, $^3H_6 \rightarrow {}^3F_4$ may be a good way to increase the intensity of 1850 nm emission.

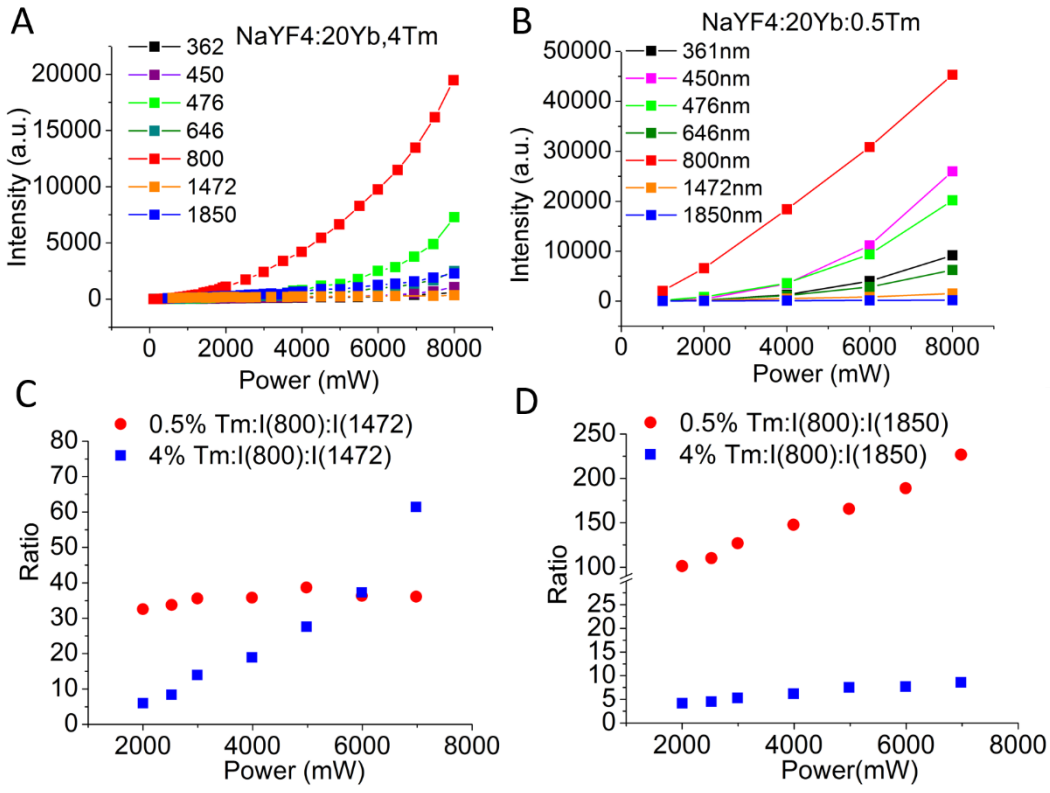

Figure 4.1.4. The diagram of emission intensity to excitation intensity for each emission peak tested from 4%Tm (A) and 0.5%Tm (B), exposure time: 500ms. (C) Intensity ratio of 800 nm to 1472 nm and (D) intensity ratio of 800 nm to 1472 nm for 4% Tm^{3+} and 0.5% Tm^{3+}. Exposure: 500ms

4.2 The influence of Gd co-doping

4.2.1 Comparison of emission spectrum

The additional dopant that mixed to original lanthanide-doped nanoparticles may affect the original emission properties. The new dopant 2% Gd is added into the sample of $NaYF_4$:20%Yb:0.5%Tm to measure the variation of spectrum and energy distribution, and the possible reasons that cause this variation will also be investigated in this section.

Figure 4.2.1 shows the spectrum from 0.5%Tm^{3+} doped nanoparticle (Left) and 2%Gd, 0.5%Tm co-doped nanoparticle (Right). From the figure, all the emission peaks in the spectrum from 0.5%Tm^{3+} doped nanoparticle appear at the same positions in the spectrum from 2%Gd, 0.5%Tm co-doped nanoparticle. In addition, the intensities of 361 nm, 450 nm, 477 nm, 646 nm, 800 nm are enhanced while the intensities of 1472 nm and 1850 nm are reduced. It appears that the additional dopant of 2% Gd help accelerate the upconversion process of Tm^{3+} ions in the sample.

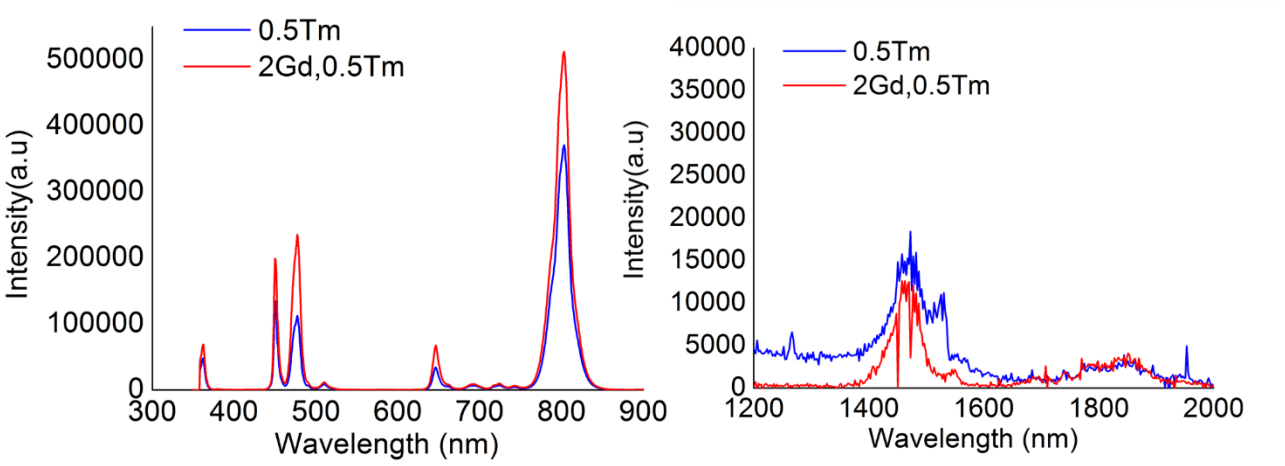

Figure 4.2.1. Comparison of UV-NIR spectrum (Left) and SWIR spectrum (Right) from 0.5% Tm^{3+} and 2% Gd, 0.5% Tm^{3+} (20% Yb^{3+}). Excitation power: 60 W/cm^2, exposure time: 6s.

4.2.2 Explore the reasons of intensity change.

As we can see (Figure 4.2.2), the energy state $^6P_{7/2}$, which represents the first excited state above the ground state $^8S_{7/2}$ of Gd^{3+} ions, has much higher energy than the excited state $^2F_{5/2}$ of Yb^{3+} ions. Therefore, the energy transfer from Yb^{3+} to Gd^{3+} to Tm^{3+} become impossible when we use 980 nm as excitation light. On the other hand, some Tm^{3+} ions at excited state $^3P_2$ can transfer its energy to the excited state $^6I_{7/2}$ of Gd^{3+} ions through process $^3P_2 \rightarrow {}^3H_6$ (Tm^{3+}), $^8S_{7/2} \rightarrow {}^6I_{7/2}$ (Gd^{3+}) due to their

appropriate energy matching [74]. Therefore, the intensities of emission peaks should reduce due to the energy transfer from Tm^{3+} to Gd^{3+}. However, the actual condition is on the contrary.

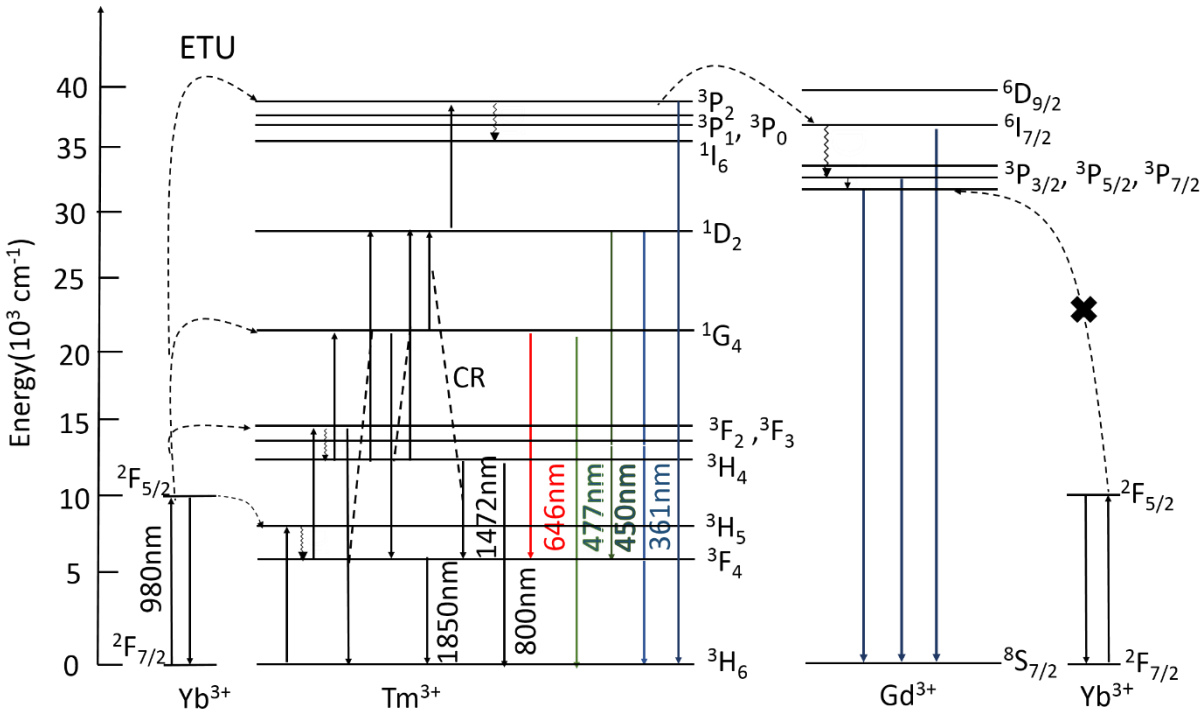

Figure 4.2.2. Energy level scheme of Yb^{3+}, Tm^{3+}, and Gd^{3+}, and possible UC processes in the sample.

To understand the effect of Gd dopant, the logarithm-logarithm diagram is measured in Figure 4.2.3. From the figure, we can know the slopes for upconversion peaks from 2% Gd, 0.5% Tm co-doped nanoparticle have same variation trend with 0.5%Tm doped nanoparticle as excitation power increases: the slopes for 361 nm, 450 nm, 800 nm are decreased while the slopes for 477 nm and 646 nm are increased after excitation intensity become larger than 11 W/cm^2 (Table 4.1). This indicates the energy transfer pathways that support luminescence may not be changed. In addition, it is found that the slope for all upconversion peaks become smaller compared with that from 0.5%Tm doped nanoparticle. According to the theory reported by Pollnau et al. in 2000 [68], the slope is reduced with larger upconversion rates in the ETU or ESA process. which matches the assumption proposed by Xie, et al. [75] that Gd dopant may help increase the electronic dipole transition probability. In order to explore the detailed reasons, additional experiments need to be done in the future.

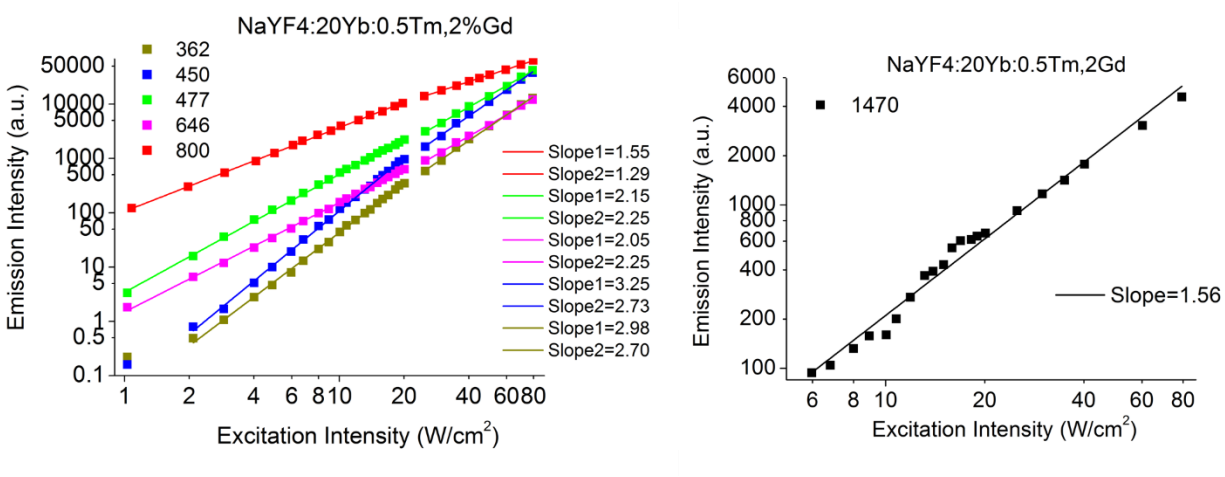

Figure 4.2.3. Logarithm-logarithm plot of emission intensity to excitation intensity for upconversion and dowconversion emission, exposure time: 500ms and 2s, respectively.

Table 4.1 The comparison of slops in logarithm-logarithm plot of emission intensity to excitation intensity between $NaYF_4$:20%Yb:0.5%Tm and $NaYF_4$:20%Yb:0.5%Tm, 2%Gd for upconversion peaks.

Emission peaks	$NaYF_4$:20%Yb:0.5%Tm	$NaYF_4$:20%Yb:0.5%Tm, 2%Gd
361 nm	3.52 → 2.89	2.98 → 2.70
450 nm	3.46 → 2.92	3.25 → 2.73
477 nm	2.35 → 2.36	2.15 → 2.25
646 nm	2.15 → 2.36	2.05 → 2.25
800 nm	1.71 → 1.35	1.55 → 1.29

4.2.3 Further validation plan

In future, firstly the high Tm concentration nanoparticle will be tested using a large excitation range to check the intensity variations of emission peaks. The intensity ratio of emission peak to overall emission will be calculated. The explanation on the dynamics of energy distribution will be explored as well.

Secondly, the reason for Gd dopant increasing the upconversion process will be checked comprehensively. Different Gd dopant concentration will be tested to examine the influence of Gd dopant on the energy distribution of emission peaks.

Thirdly, the lifetime of emission peaks will be measured using the time-detection system to help confirm the dominant energy transfer pathways.

4.3 Remarks

In this chapter, the spectrum of high Tm doping concentration nanoparticle and Tm/Gd co-doped nanoparticle are measured and compared with low Tm doping concentration nanoparticle to find out the difference on energy distribution of emission peaks. For high Tm doping concentration nanoparticle, the possible reason for the increased intensity of 1850 nm, that is the additional pathways induced by high Tm doping, is described. The intensity ratio of 800 nm to 1471 nm and 800 nm to 1850 nm are compared with low Tm doping nanoparticles to help explain the energy distribution variation of downconversion peaks, although the influence on energy distribution of upconversion peaks cannot be explained due to the insufficient excitation intensity. For Gd/Tm co-doped nanoparticle, the possible reason for the increased intensity of emission peaks 361 nm, 450 nm, 477 nm, 646 nm, 800 nm is proposed as the improvement of electronic dipole transition probability rather than changing the energy transfer pathways within Tm^{3+} ions.

5
Conclusion and perspectives

5.1 Conclusions

In this research work, firstly I developed a low-cost and ultra-broad spectrum measurement system by integrating visible spectrometer #USB2000+ and NIR spectrometer #NIRQuest512. Combining the system with proposed experiment method, the entire spectra of Er^{3+} and Tm^{3+} doped nanoparticles were measured.

Secondly, I investigated the detailed photon conversion processes in typical lanthanide doped nanoparticles $NaYF_4:Yb^{3+}:Er^{3+}$ and $NaYF_4:Yb^{3+}:Tm^{3+}$. The measured spectrum shows that $NaYF_4:Yb^{3+}:Er^{3+}$ has emission peaks 525 nm, 545 nm, 655 nm, 1525 nm, which are created by the energy transitions $^2H_{11/2} \rightarrow {}^4I_{15/2}$, $^4S_{3/2} \rightarrow {}^4I_{15/2}$, $^4F_{9/2} \rightarrow {}^4I_{15/2}$, and $^4I_{13/2} \rightarrow {}^4I_{15/2}$, respectively, while the $NaYF_4:Yb^{3+}$, Tm^{3+} has emission peaks 361 nm, 450 nm, 477 nm, 646 nm, 800 nm and 1472nm, which are created by the energy transitions $^1D_2 \rightarrow {}^3H_6$, $^1D_2 \rightarrow {}^3F_4$, $^1G_4 \rightarrow {}^3H_6$, $^1G_4 \rightarrow {}^3F_4$, $^3H_4 \rightarrow {}^3H_6$, and $^3H_4 \rightarrow {}^3F_4$. By investigating both slope value in power-dependent luminescence diagram and energy gap in energy-level diagram, the different dominant energy pathways that populate the energy transitions are interpreted, which are shown in Figure 3.2.6, Figure 3.2.7, Figure 3.3.5 and Figure 3.3.6. Regarding energy distribution, the emission efficiency of downconversion peak 1525 nm reduces as excitation intensity increases for $NaYF_4:Yb^{3+}:Er^{3+}$. On the other hand, the emission efficiency of 1472 nm continues to increase as excitation intensity increases for $NaYF_4:Yb^{3+}:Tm^{3+}$, which would be a good prerequisite for SWIR luminescence although the quantity-yield is still low.

Thirdly, in order to find the approaches to improve the intensities of specific emission wavelengths especially in the SWIR region, I compared the energy distribution of emission peaks between 4% Tm doped nanoparticle $NaYF_4:Yb^{3+}:Tm^{3+}$ and 0.5% Tm doped nanoparticle $NaYF_4:Yb^{3+}:Tm^{3+}$ as well as 2% Gd, 0.5% Tm co-doped nanoparticle $NaYF_4:Yb^{3+}:Tm^{3+}$, Gd^{3+}. The result shows that increasing Tm concentration will help increase the intensity of downconversion emission as long as the excitation power is satisfied. However, the additional 2% Gd dopant will inversely help increase the

energy distribution of upconversion emission probably by the improvement of electronic dipole transition probability. Further work for validation are mentioned.

5.2 Perspectives

The goal of this research work is to find the key factors that dominate the luminescence enhancement and to select the most promising choices(s) that can be used for SWIR fluorescence. In future, a series of different concentrations of Er- and Tm- doped nanoparticles (different ratio of Yb:Er or Tm) will be tested under a large range of excitation intensity to inspect their luminescence in order to find the most intense lanthanide doping concentration for SWIR emission.

Moreover, I want to explore the influence of lanthanide doping concentration on the lifetime of photoluminescence. Since the lifetime of photoluminescence can be tuned from tens of nanosecond to a few microseconds by controlling the dopant and doping concentration, the lifetime-multiplexing become a good way to distinguish different luminescence. Compared to the colour-multiplexing, lifetime-multiplexing reduces the colour affection from the scattering light and autofluorescence, therefore is a more robust way for in vivo imaging.

Furthermore, I want to develop a time-gating imaging system that has the ability to block-open the excitation light in the microsecond period. Combining the time-gating system with the long lifetime of lanthanide nanoparticles, the imaging contrast can be extremely improved due to the disappearance of scattering light and autofluorescence.

References

1. Naumova, A.V., et al., *Clinical imaging in regenerative medicine.* Nature Biotechnology, 2014. **32**(8): p. 804.
2. Ntziachristos, V., et al., *Looking and listening to light: the evolution of whole-body photonic imaging.* Nature Biotechnology, 2005. **23**(3): p. 313.
3. Etrych, T., et al., *Fluorescence optical imaging in anticancer drug delivery.* Journal of Controlled Release, 2016. **226**: p. 168.
4. Weissleder, R., *A clearer vision for in vivo imaging.* Nature Biotechnology, 2001. **19**: p. 316.
5. Bashkatov, A., et al., *Optical properties of human skin, subcutaneous and mucous tissues in the wavelength range from 400 to 2000 nm.* Journal of Physics D: Applied Physics, 2005. **38**(15): p. 2543.
6. Lim, Y.T., et al., *Selection of quantum dot wavelengths for biomedical assays and imaging.* Molecular Imaging, 2003. **2**(1): p. 50.
7. Ntziachristos, V., *Going deeper than microscopy: the optical imaging frontier in biology.* Nature Methods, 2010. **7**(8): p. 603.
8. Smith, A.M., et al., *Bioimaging: second window for in vivo imaging.* Nature Nanotechnology, 2009. **4**(11): p. 710.
9. Hong, G., et al., *Near-infrared fluorophores for biomedical imaging.* Nature Biomedical Engineering, 2017. **1**(1): p. 0010.
10. Desmettre, et al., *Fluorescence properties and metabolic features of indocyanine green (ICG) as related to angiography.* Survey of Ophthalmology, 2000. **45**(1): p. 15.
11. Tanaka, E., et al., *Real-time assessment of cardiac perfusion, coronary angiography, and acute intravascular thrombi using dual-channel near-infrared fluorescence imaging.* The Journal of Thoracic and Cardiovascular Surgery, 2009. **138**(1): p. 133.
12. Tao, Z., et al., *Biological imaging using nanoparticles of small organic molecules with fluorescence emission at wavelengths longer than 1000 nm.* Angewandte Chemie, 2013. **125**(49): p. 13240.
13. Antaris, A.L., et al., *A small-molecule dye for NIR-II imaging.* Nature Materials, 2016. **15**(2): p. 235.
14. Heuveling, D.A., et al., *Nanocolloidal albumin-IRDye 800CW: a near-infrared fluorescent tracer with optimal retention in the sentinel lymph node.* European Journal of Nuclear Medicine And Molecular Imaging, 2012. **39**(7): p. 1161.

15. Zheng, X., et al., *High-Contrast Visualization of Upconversion Luminescence in Mice Using Time-Gating Approach.* Analytical Chemistry, 2016. **88**(7): p. 3449.
16. Troyan, S.L., et al., *The FLARE™ intraoperative near-infrared fluorescence imaging system: a first-in-human clinical trial in breast cancer sentinel lymph node mapping.* Annals of Surgical Oncology, 2009. **16**(10): p. 2943.
17. van der Vorst, J.R., et al., *Near‐infrared fluorescence‐guided resection of colorectal liver metastases.* Cancer, 2013. **119**(18): p. 3411.
18. Frangioni, J.V., *In vivo near-infrared fluorescence imaging.* Current Opinion In Chemical Biology, 2003. **7**(5): p. 626.
19. Nakayama, A., et al., *Quantitation of brown adipose tissue perfusion in transgenic mice using near-infrared fluorescence imaging.* Molecular Imaging, 2003. **2**(1): p. 5.
20. Welsher, K., et al., *Deep-tissue anatomical imaging of mice using carbon nanotube fluorophores in the second near-infrared window.* Proceedings of the National Academy of Sciences, 2011. **108**(22): p. 8943.
21. Liu, H., et al., *Fluorescent carbon nanoparticles derived from candle soot.* Angewandte Chemie, 2007. **119**(34): p. 6593.
22. He, X., et al., *Water soluble carbon nanoparticles: hydrothermal synthesis and excellent photoluminescence properties.* Colloids and Surfaces B: Biointerfaces, 2011. **87**(2): p. 326.
23. Tao, H., et al., *In vivo NIR fluorescence imaging, biodistribution, and toxicology of photoluminescent carbon dots produced from carbon nanotubes and graphite.* Small, 2012. **8**(2): p. 281.
24. Kong, B., et al., *Carbon dot‐based inorganic–organic nanosystem for two‐photon imaging and biosensing of pH variation in living cells and tissues.* Advanced Materials, 2012. **24**(43): p. 5844.
25. Leeuw, T.K., et al., *Single-walled carbon nanotubes in the intact organism: near-IR imaging and biocompatibility studies in Drosophila.* Nano Letters, 2007. **7**(9): p. 2650.
26. Hong, G., et al., *Carbon Nanomaterials for Biological Imaging and Nanomedicinal Therapy.* Chemical Review, 2015. **115**(19): p. 10816.
27. Welsher, K., et al., *Selective probing and imaging of cells with single walled carbon nanotubes as near-infrared fluorescent molecules.* Nano Letters, 2008. **8**(2): p. 586.
28. Welsher, K., et al., *A route to brightly fluorescent carbon nanotubes for near-infrared imaging in mice.* Nature Nanotechnology, 2009. **4**(11): p. 773.

29. Tabakman, S.M., et al., *Optical properties of single-walled carbon nanotubes separated in a density gradient: length, bundling, and aromatic stacking effects.* The Journal of Physical Chemistry C, 2010. **114**(46): p. 19569.
30. Ju, S.-Y., et al.. Papadimitrakopoulos, *Brightly fluorescent single-walled carbon nanotubes via an oxygen-excluding surfactant organization.* Science, 2009. **323**(5919): p. 1319.
31. Hong, G., et al., *Multifunctional in vivo vascular imaging using near-infrared II fluorescence.* Nature Medicine, 2012. **18**(12): p. 1841.
32. Liu, Z., et al., *Carbon nanotubes in biology and medicine: in vitro and in vivo detection, imaging and drug delivery.* Nano Research, 2009. **2**(2): p. 85.
33. Wang, X., et al., *Carbon nanotubes in biology and medicine: An overview.* Chinese Science Bulletin, 2012. **57**(2-3): p. 167.
34. Gaponik, N., et al., *Labeling of biocompatible polymer microcapsules with near-infrared emitting nanocrystals.* Nano Letters, 2003. **3**(3): p. 369.
35. Tsay, J.M., et al., *Hybrid approach to the synthesis of highly luminescent CdTe/ZnS and CdHgTe/ZnS nanocrystals.* Journal of the American Chemical Society, 2004. **126**(7): p. 1926.
36. Yong, K.T., et al., *Biocompatible near‐infrared quantum dots as ultrasensitive probes for long‐term in vivo imaging applications.* Small, 2009. **5**(17): p. 1997.
37. Du, Y., et al., *Near-infrared photoluminescent Ag2S quantum dots from a single source precursor.* Journal of the American Chemical Society, 2010. **132**(5): p. 1470.
38. Hong, G., et al., *In vivo fluorescence imaging with Ag2S quantum dots in the second near‐infrared region.* Angewandte Chemie International Edition, 2012. **51**(39): p. 9818.
39. Zhang, Y., et al., *Ag2S quantum dot: a bright and biocompatible fluorescent nanoprobe in the second near-infrared window.* ACS nano, 2012. **6**(5): p. 3695.
40. Kim, S.-W., et al., *Engineering InAs x P1-x/InP/ZnSe III− V Alloyed Core/Shell Quantum Dots for the Near-Infrared.* Journal of the American Chemical Society, 2005. **127**(30): p. 10526.
41. Aharoni, A., et al., *Synthesis of InAs/CdSe/ZnSe core/shell1/shell2 structures with bright and stable near-infrared fluorescence.* Journal of the American Chemical Society, 2006. **128**(1): p. 257.
42. Liu, X., et al., *Tumor-Targeted Multimodal Optical Imaging with Versatile Cadmium-Free Quantum Dots.* Advanced Functional Materials, 2016. **26**(2): p. 267.
43. Wegner, K.D., et al., *Quantum dots: bright and versatile in vitro and in vivo fluorescence imaging biosensors.* Chemical Society Reviews, 2015. **44**(14): p. 4792.

44. Chung, J.W., et al., *Recent advances in luminescence properties of lanthanide-doped up-conversion nanocrystals and applications for bio-imaging, drug delivery, and optosensing.* Applied Spectroscopy Reviews, 2016. **51**(7-9): p. 678.
45. Wang, F., et al., *Recent advances in the chemistry of lanthanide-doped upconversion nanocrystals.* Chemical Society Reviews, 2009. **38**(4): p. 976.
46. Wang, F., et al., *Tuning upconversion through energy migration in core–shell nanoparticles.* Nature Materials, 2011. **10**(12): p. 968.
47. Zhang, F., et al., *Fluorescence upconversion microbarcodes for multiplexed biological detection: nucleic acid encoding.* Advanced Materials, 2011. **23**(33): p. 3775.
48. Zhang, Y., et al., *Multicolor barcoding in a single upconversion crystal.* Journal of the American Chemical Society, 2014. **136**(13): p. 4893.
49. Wang, J., et al., *Single‐band upconversion emission in lanthanide‐doped KMnF3 nanocrystals.* Angewandte Chemie, 2011. **123**(44): p. 10553.
50. Wang, Y.-F., et al., *Nd3+-sensitized upconversion nanophosphors: efficient in vivo bioimaging probes with minimized heating effect.* ACS Nano, 2013. **7**(8): p. 7200.
51. Dejneka, M.J., et al., *Rare earth-doped glass microbarcodes.* Proceedings of the National Academy of Sciences, 2003. **100**(2): p. 389.
52. Wang, F., et al., *Upconversion multicolor fine-tuning: visible to near-infrared emission from lanthanide-doped NaYF4 nanoparticles.* Journal of the American Chemical Society, 2008. **130**(17): p. 5642.
53. Johnson, N.J., et al., *Size-tunable, ultrasmall NaGdF4 nanoparticles: insights into their T1 MRI contrast enhancement.* Chemistry of Materials, 2011. **23**(16): p. 3714.
54. Nyk, M., et al., *High contrast in vitro and in vivo photoluminescence bioimaging using near infrared to near infrared up-conversion in Tm3+ and Yb3+ doped fluoride nanophosphors.* Nano Letters, 2008. **8**(11): p. 3834.
55. Xie, X., et al., *Mechanistic investigation of photon upconversion in Nd3+-sensitized core–shell nanoparticles.* Journal of the American Chemical Society, 2013. **135**(34): p. 12608.
56. Wang, F., et al., *Facile synthesis of water-soluble LaF 3 ∴ Ln 3+ nanocrystals.* Journal of Materials Chemistry, 2006. **16**(11): p. 1031.
57. Yu, X.F., et al., *Highly efficient fluorescence of NdF3/SiO2 core/shell nanoparticles and the applications for in vivo NIR detection.* Advanced Materials, 2008. **20**(21): p. 4118.
58. Naczynski, D., et al., *Rare-earth-doped biological composites as in vivo shortwave infrared reporters.* Nature Communications, 2013. **4**: p. 2199.

59. Zheng, X., et al., *High-contrast visualization of upconversion luminescence in mice using time-gating approach.* Analytical Chemistry, 2016. **88**(7): p. 3449.
60. Dieke, G.H., et al., *The spectra of the doubly and triply ionized rare earths.* Applied Optics, 1963. **2**(7): p. 675.
61. Zhan, Q., et al., *Achieving high-efficiency emission depletion nanoscopy by employing cross relaxation in upconversion nanoparticles.* Nature Communications, 2017. **8**(1): p. 1058.
62. Carnall, W., et al., *A systematic analysis of the spectra of the lanthanides doped into single crystal LaF3.* The Journal of Chemical Physics, 1989. **90**(7): p. 3443.
63. Carnall, W., et al., *Electronic energy levels in the trivalent lanthanide aquo ions. I. Pr3+, Nd3+, Pm3+, Sm3+, Dy3+, Ho3+, Er3+, and Tm3+*. The Journal of Chemical Physics, 1968. **49**(10): p. 4424.
64. Carnall, W., et al., *Energy level structure and transition probabilities in the spectra of the trivalent lanthanides in LaF_3*. 1978, Argonne National Lab.(ANL), Argonne, IL (United States).
65. Cao, B., et al., *Upconversion properties of Er3+–Yb3+: NaYF4 phosphors with a wide range of Yb3+ concentration.* Journal of Luminescence, 2013. **135**: p. 128.
66. Würth, C., et al., *Excitation power dependent population pathways and absolute quantum yields of upconversion nanoparticles in different solvents.* Nanoscale, 2017. **9**(12): p. 4283.
67. Zhao, J., et al., *Upconversion luminescence with tunable lifetime in NaYF 4: Yb, Er nanocrystals: role of nanocrystal size.* Nanoscale, 2013. **5**(3): p. 944.
68. Pollnau, M., et al., *Power dependence of upconversion luminescence in lanthanide and transition-metal-ion systems.* Physical Review B, 2000. **61**(5): p. 3337.
69. Hu, S., et al., *Upconversion Luminescence and Magnetic Turning of NaLu [F. sub. 4]:[Yb. sup. 3+]/[Tm. sup. 3+]/[Gd. sup. 3+] Nanoparticles and Their Application for Detecting Acriflavine.* Journal of Nanomaterials, 2016.
70. Dong, H., et al., *Basic understanding of the lanthanide related upconversion emissions.* Nanoscale, 2013. **5**(13): p. 5703.
71. Zhao, J., et al., *Single-nanocrystal sensitivity achieved by enhanced upconversion luminescence.* Nature Nanotechnology, 2013. **8**(10): p. 729.
72. Wang, G., et al., *Intense ultraviolet upconversion luminescence from hexagonal NaYF 4: Yb 3+/Tm 3+ microcrystals.* Optics Express, 2008. **16**(16): p. 11907.
73. Noginov, M., et al., *Excitation scheme for the upper energy levels in a Tm: Yb: BaY 2 F 8 laser crystal.* JOSA B, 1997. **14**(8): p. 2126.

74. Cao, C., et al., *Ultraviolet upconversion emissions of Gd 3+*. Optics Letters, 2008. **33**(8): p. 857.
75. Xie, W., et al., *Tunable phase and upconverting luminescence of Gd3+ co-doped NaErF4: Yb3+ nanostructures.* Materials Research Bulletin, 2017. **95**: p. 509.